ORIGINAL ARTICLE

Manufacturing constrained shape optimisation of variable width flat web formed channels

Jie Gong[1] · Kazem Ghabraie[1] · Matthias Weiss[2] · Achuth Sreenivas[2] · Bernard Rolfe[1]

Abstract

The trend in automotive manufacturing towards lower volumes and an increased number of car variants combined with the need for forming higher strength metals to reduce weight has led to the implementation of alternative and flexible manufacturing methods. These have new manufacturing constraints compared to conventional stamping that change the part shapes that can be formed. This requires new methods for part shape optimisation. This study proposes a novel parametrisation for shape design that allows: 1) implementation of a gradient-based optimisation approach; and 2) taking manufacturing constraints into account. Our novel parameterisation can describe most long automotive structural parts using only a small number of design variables. The parts are described using multiple series of straight and curved connected profiles. We have uniquely conducted a detailed sensitivity analysis on the profiles to determine analytical solutions for the first order derivatives of the design variables with respect to the surface area/mass of a generic part. The profiles are also used to determine the final manufacturing strains in a part based on ideal forming. These ideal manufacturing strains can be compared to manufacturing process strain limits to determine the potential manufacturability of the part. The proposed parametrisation is applied to optimise a variable width channel formed by flexible roll forming. The channel is optimised to maximise the stiffness while maintaining both mass and manufacturability. In detail, the effectiveness and the general applicability of the established parametrisation technique and shape optimisation platform are demonstrated using three case studies of a flexible roll formed automotive S-rail channel part subjected to compression and bending loads. Furthermore, the manufacturability of the optimised structure is demonstrated by a forming model of the flexible roll forming process, where the model has been previously validated against experimental data. These examples show that the presented parametrisation and the associated shape optimiser can be successfully applied to increase part stiffness while reducing weight and maintaining manufacturability. The range of problems analysed demonstrates the flexibility and capability of the newly developed optimisation platform.

Keywords Shape optimisation · Parametric model · Flexible roll forming · Manufacturing constraints · Newton-like interior-point method

1 Introduction

Automotive companies are pursuing lightweight structures with high strength materials to reduce carbon dioxide emission and fuel consumption while meeting the strength requirements [1]. This is combined with a shift towards flexible manufacturing to enable the cost-effective production of multiple electric vehicle variants at lower volumes on the same platform. Conventional stamping does not allow the forming of new high-performance materials that often combine high strength with limited ductility. Hot stamping can form high strength steels but requires high infrastructure investment [2, 3] and only allows production of one component shape per tool set. New forming processes have therefore been implemented. These are often limited to the forming of different component shapes than those that are conventionally producible with stamping. This requires the manufacturable design and optimisation of new shapes that lead to similar or enhanced structural performance compared to the complex stamped counterparts while at the same time suiting the manufacturing constraints of the new process.

✉ Bernard Rolfe
bernard.rolfe@deakin.edu.au

1 School of Engineering, Deakin University, Pigdons Rd, Waurn Ponds, VIC 3216, Australia

2 Institute for Frontier Materials, Deakin University, Pigdons Rd, Waurn Ponds, VIC 3216, Australia

Shape optimisation is an efficient design tool for thin-walled structures for identifying the design satisfying crash and structural performance requirements in comparison to trial-and-error approaches. The mechanical properties of thin-walled channels and tubes mainly rely on the cross-sectional geometry. Investigations on straight beams with constant cross-section along the longitudinal axis [4], including circle [5], square [6, 7], triangular [8], multi-corner [9], start shape [10], and polygonal tubes [11–13] have been conducted in previous studies. Simple geometrical changes along the axis such as tapering and conical tubes were also analysed to exploit further potential in lightweight and stiffness improvement [14–21].

However, the increasing functionality and assembly have demanded interests in long components with curved axes and variable cross sections. The mesh morphing technique was used to account for complex shape variations by relocating the nodes to modify the element during the optimisation process [22], however this technique is limited to small shape changes, as otherwise the finite element mesh will distort. To solve this issue, an implicit parametrisation modelling technique in SFE-CONCEPT was established [23]. In this method, the variable cross-sectional structure is represented by baselines, base sections and control points. Adjacent arbitrary cross sections are connected along the baseline in the longitudinal direction and the baselines are varied by control points [24, 25]. Hilmann [26] integrated the implicit parametrisation technique into the shape optimisation process where the viability was tested by optimising a front bumper system using a Genetic Algorithm (GA). Duan et al. [27] developed a lightweight strategy for a body-in-white concept using a global sensitivity analysis coupled with the SFE-CONCEPT. In their work, the design space complexity reduction was conducted by using the global sensitivity analysis (GSA) technique and a response surface method model (RSMM). Cai and Wang [28] combined the grey relational analysis technique and grey entropy measurement method to optimise an SFE-CONCEPT modelled S-rail. Xie and Wang [29] optimised a cross-sectional S-rail with and without reinforcement using the commercial SFE-CONCEPT in combination with a multi-objective optimisation process. The similar finite element mesh model, which decomposes the variable slender component into global and local deformation were proposed by Yang et al. [30] and validated numerically by Hu et al. [31].

Although the implicit method with the SFE CONCEPT can form curved tubes, it only has been used for shape optimisation to a limited extend. There are three main reasons for this. First, a large set of design variables, including cross sections, base points and base lines, need to be considered to describe longitudinal parts that have a variable cross section over the length. Therefore, reducing the number of design variables is usually conducted before optimisation [27], which may result in failing to explore all relevant shape configurations. Secondly, as the sensitivity information cannot be calculated with the SFE

CONCEPT, non-gradient-based methods, such as metaheuristic algorithms, are usually selected as the optimisation solvers. For one of the widely used metaheuristic algorithms, GA, it requires orders of magnitude more function evaluations compared with gradient-based optimisation approaches [32, 33]. GA generates design variables randomly and executes multiple simulations based on the demanded size of the population at each iteration. This results in high computational costs. In addition, the results of GA highly depend on the way of formulating the cost function and the selected rate of crossover and mutation operators [34–36]. Although the same parameters are defined, the randomness of GA still causes difficulties in reproducing the same optimised results. In contrast, the gradient-based algorithm can reproduce the same optimised results while using the same parameter settings since the sensitivities calculated based on the proposed parametrisation technique provide a deterministic descent direction [37]. Meanwhile, the simulation only needs to be executed once for the objective function evaluation at each iteration in the gradient-based optimisation process. Third, besides the metaheuristic algorithms, statistical techniques, such as response surface methods, are also widely used for shape optimisation because of no requirements of sensitivities. However, every set of the input design variables and output results needs to be modified and collected by users. It is a manual method that is time-consuming compared to other automatic methods [27].

This work therefore proposes a flexible and more efficient shape parametrisation for complex channel shapes that requires only a small set of design variables while capable of formulating manufacturing constraints. This allows using a modified Newton-like interior point optimisation method, that is more robust and efficient than GA. The optimisation platform is established using the sensitivity derived from the proposed parametrisation method, to optimise mechanical performance under the weight constraint. Geometrical and manufacturing constraints are considered to ensure that the optimised cross sections can be successfully modelled and manufactured with the designated manufacturing process.

The approach is developed and applied to the new Flexible Roll Forming (FRF) process but can also be transferred to other manufacturing processes if required. FRF was chosen because it enables cost-efficient manufacture of automotive parts from high strength metal sheet, including bumpers, door beams, roof bows and frame rails [38–43]. Unlike conventional roll forming process where the forming rolls are mounted on fixed stands to form constant cross-sectional parts, the forming rolls in FRF can rotate and move to follow a complex part contour, as schematically shown in Fig. 1. This enables the manufacture of full families of long components with variable width and depth over the length of the part with only one tool set. This promises reduced manufacturing costs and higher product flexibility.

Fig. 1 Movement of the roll tooling in FRF with width variation
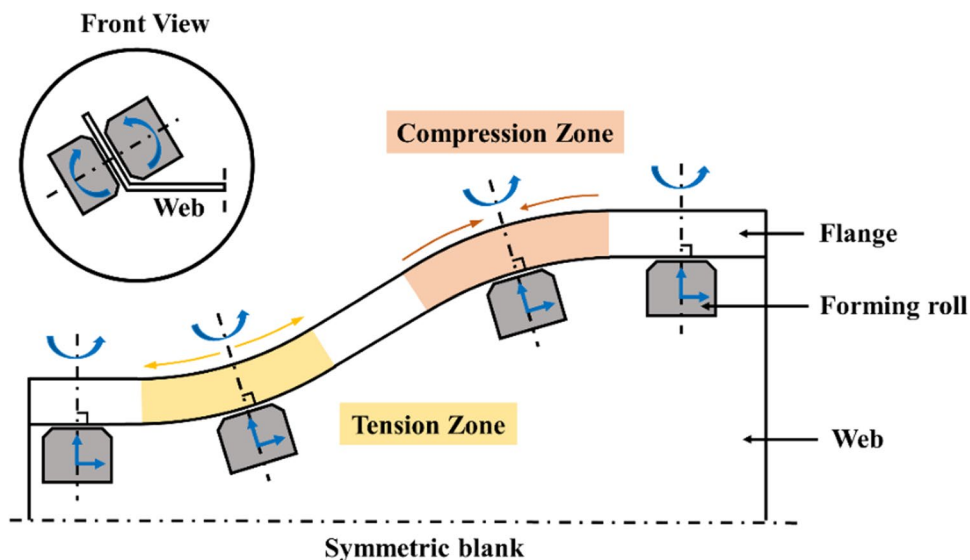
The problem is that when the concave and convex zones are formed, longitudinal tensile and compressive strains and stresses occur in the flange (Fig. 1). This can result in shape defects such as web warping (deviation in height of the web) and wrinkling (waving in the flange) [44, 45]. Previous studies have been limited to the development of tool solutions such as blank holders [46] and special forming rolls [47, 48] or have aimed at optimising the forming sequence [49] to eliminate the defects. Recent studies have developed relationships between the process parameters and the defect initiation, and proposed analytical equations to estimate the strain limits during manufacturing [50–55]. This has produced a fundamental platform for optimising part performance of FRF parts while at the same time accounting for manufacturing constraints to prevent defect formation.

2 Concept of the Proposed Parametrisation

As discussed in Section 1, the parametrisation can affect the selection of the optimiser, and this is directly related to the rate of convergence. Generic examples of flat channels with variable width are demonstrated in Fig. 2. The web of these

channels is made of straight and curved sections. The proposed parametrisation approach directly defines the contours of the web using a number of control circles, and then finding the tangential envelope. This is demonstrated in Fig. 3.

In this parametrisation, the i_{th} transitional arc is fully represented by the coordinates of the circle centre in the Cartesian coordinate system with the length - x_i, the width - y_i, and the radius of the transitional part - r_i. These three values are grouped as one triplet in this method. Depending on the positive or the negative value of r_i, the direction of the arc will be convex or concave respectively after connecting the straight sections. If $r_i = 0$, the transitional section merges to one point. From these triplets (x_i, y_i, r_i), all points of tangency ($P_{i,j}$ in Fig. 3), which form the contour of the part, can be calculated based on the relationship of two arcs (refer to Appendix A for more details).

There are four sets of design variables including the 12 coordinates in Fig. 3. Based on the definition of the parametrisation method, $r_0 = r_4 = 0$, r_1 and r_2 are negative and positive, respectively. Three straight sections and two transitional sections are connected by six points of tangency ($P_{i,j}$). With this method, the shape configuration of parts can be modified by changing the coordinates of the design variables. More complicated channels can be analysed by adding

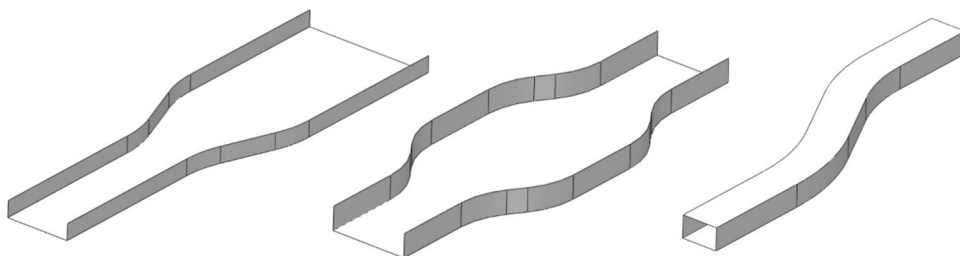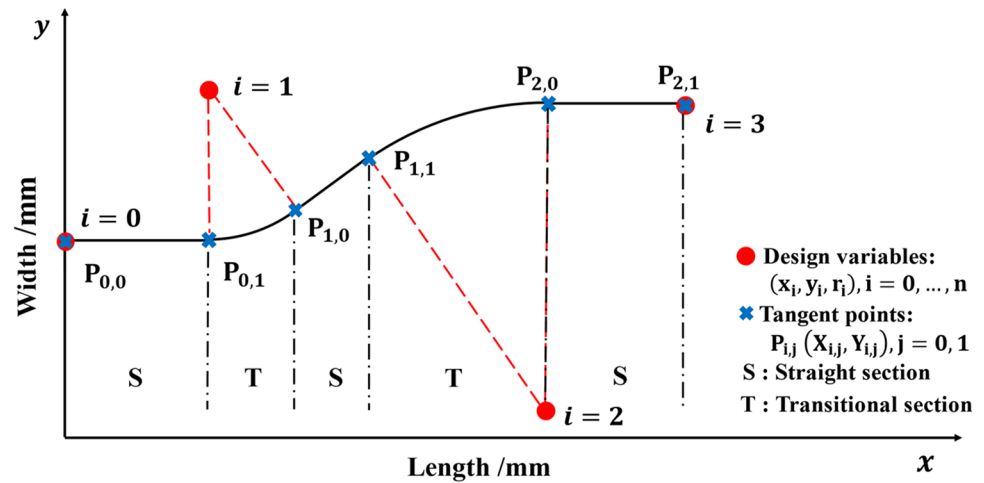**Fig. 2** Channels with variable width cross sections

Fig. 3 Geometrical model demonstrating the proposed parametric method

additional sets of coordinates. Utilising this parametric method, any combination of potential channels with a variable width cross section can be represented. Most importantly, the small number of design variables in this parametrisation allows usage of gradient-based optimisation techniques.

3 FRF and Manufacturing Constraints

The mechanics of the manufacturing constraints of FRF mentioned above are illustrated in Fig. 4. In the FRF process, the sheet metal strips are bent incrementally by the rollers to form variable cross sections along the feeding direction. The bend curves in the transitional section of the pre-cut blank are $a_1b_1 < a_2b_2$ and $c_1d_1 > c_2d_2$. To include a bend angle, the final bend curve must be subjected to the condition of $a_1b_1 = a_2b_2$ and $c_1d_1 = c_2d_2$. Therefore, the initial bend curve a_1b_1 is stretched to a_2b_2, and c_1d_1 is compressed to c_2d_2 after FRF [54]. To maintain a defect-free structure,

the tension and compression in the transitional sections need to be less than the tearing or wrinkling limit of the material, respectively, otherwise forming defects will occur [56, 57].
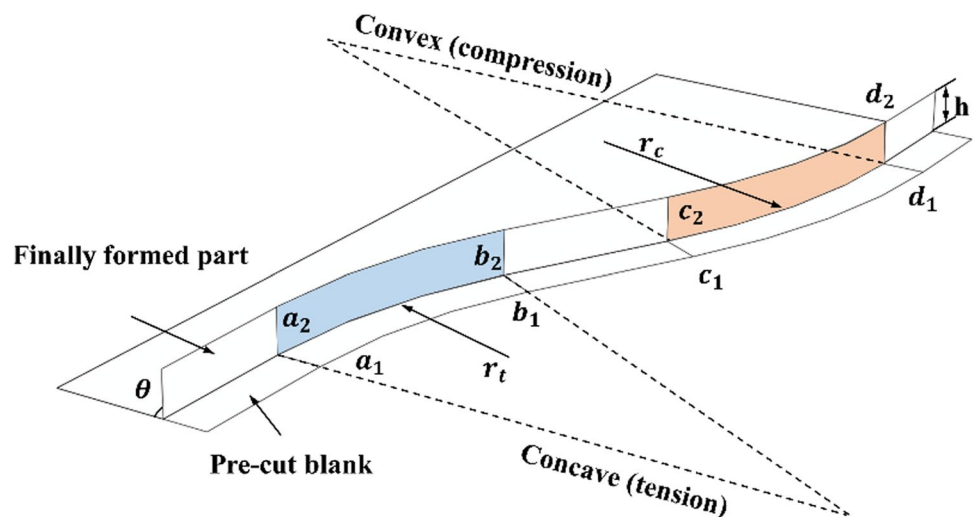
The following analytical equations, based on ideal forming conditions, can be used to determine the forming strains [54]:

$$\varepsilon_t = \ln\left(1 + \frac{h(1 - \cos(\theta))}{r_t - h}\right) \qquad (1)$$

$$\varepsilon_c = \ln\left(1 - \frac{h(1 - \cos(\theta))}{r_c + h}\right) \qquad (2)$$

where ε_t and ε_c are the predicted longitudinal strains for tension and compression in the concave and convex zones, respectively; θ and h are the bend angle and flange height; r_t and r_c are the transitional radii of the tension and compression sections in the final part (Fig. 4). Following Eqs. (1) and (2), the manufacturing constraints are defined as:

Fig. 4 Schematic of the symmetric half of the FRF channel with variable width cross section

$$g_{ten} = \ln\left(1 + \frac{h(1 - \cos(\theta))}{r_t - h}\right) - \hat{\varepsilon}_t \le 0 \tag{3}$$

$$g_{com} = \left|\ln\left(1 - \frac{h(1 - \cos(\theta))}{r_c + h}\right)\right| - |\hat{\varepsilon}_c| \le 0 \tag{4}$$

where $\hat{\varepsilon}_t$ and $\hat{\varepsilon}_c$ are the longitudinal strain limits for tension and compression in the transitional sections, respectively.

4 Using the Proposed Parametrisation to Describe FRF Parts

The proposed parametrisation can efficiently capture the characteristics of the FRF shape modes with a small number of design variables. The feature of variable width FRF parts (similar as Fig. 2) can be represented by transitional sections in form of arcs of circles that are connected by

the tangents of these circular arcs. Besides, the manufacturing constraints of FRF discussed in Section 3 (Eqs. (3) and (4)) can be easily formulated and controlled as the radii r_t and r_c are among the design variables.

4.1 Design Variables

Based on the parametric method demonstrated above, a general FRF channel with complex variable width cross sections is established in Fig. 5. The profile of the variable width channel is represented by the line and curve sections. As the profile is not symmetric and the design domains of the transitional radii in the concave (tension) and convex (compression) zones are different, the upper and lower profiles of the structure are analysed and modelled independently.

The upper and lower profiles of the channel in Fig. 5 are formed by six and seven triplets of design variables, separately. All design variables can be expressed as:

Fig. 5 A variable width channel modelled by the proposed parametric method, (a). Upper and lower design variables in channel (ru_2, ru_3, rl_1 and rl_4 are positive, ru_1, ru_4, rl_2, rl_3 and rl_5 are negative, and ru_0, ru_5, rl_0 and rl_6 are equal to zero), (b). A channel with variable cross sections in width
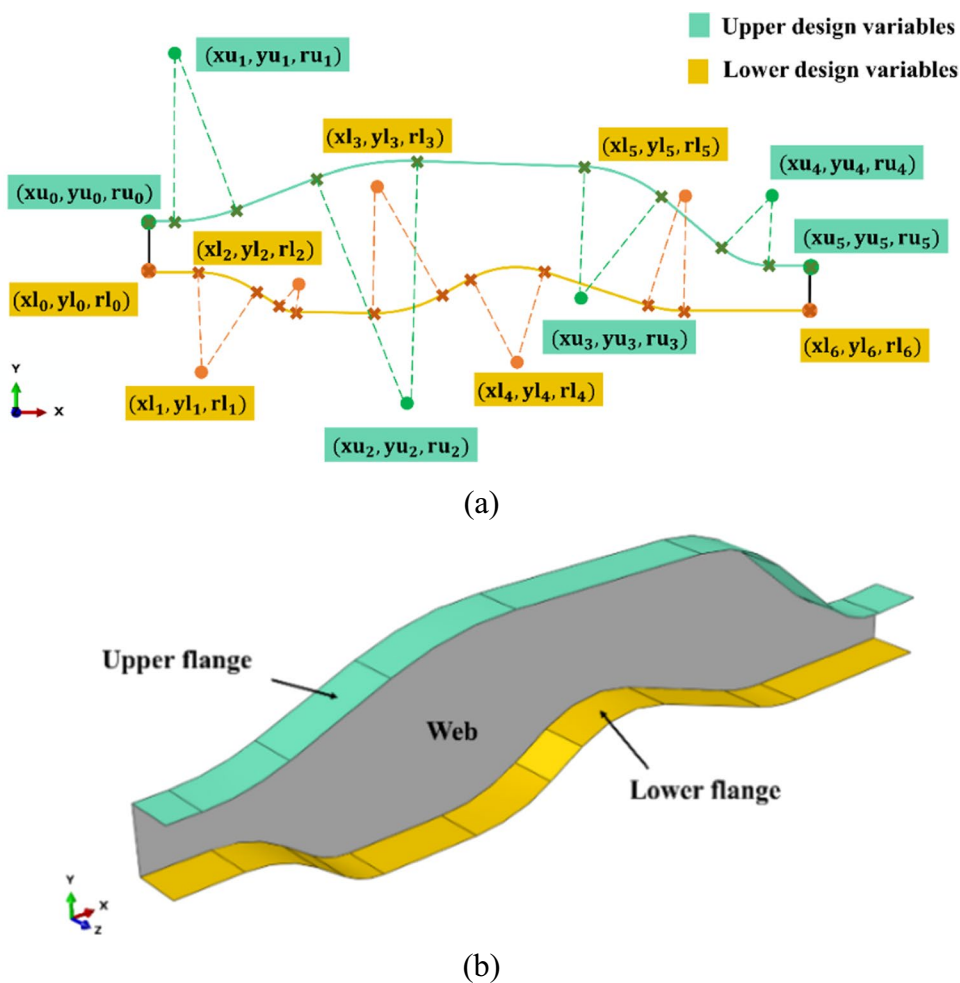
$$X = \left[xu_i, yu_i, ru_i, xl_j, \ \ yl_j, rl_j \ \right]^T (i = 0, \dots, p, j = 0, \dots, q) \tag{5}$$

where (xu_i, yu_i, ru_i) represents the design variables of the upper contour and (xl_j, yl_j, rl_j) represents the design variables of the lower contour. For this model, p is equal to 5 and q is equal to 6. The vector of the design variables can be expressed in a general form:

$$X = \left[x_0, \dots, x_n \ \right]^T \ (n = p + q) \tag{6}$$

During the optimisation process, the shape configuration of the part and the manufacturing constraints can be easily controlled by changing the values of the design variables.

5 Formulation of the Optimisation Problem and Sensitivity Analysis

5.1 Objective Function

The aim of this study is to optimise the structural performance of the channel under the relevant loading conditions by minimising the strain energy (compliance) while maintaining the manufacturability. Minimising strain energy or

compliance will result in stiffer designs which is generally desirable in automotive parts. The objective function is given as a function of the design vector X which has the form:

$$\min f(X) \ \left(\ LB_{x_i} \le x_i \le UB_{x_i} \right)(i = 0, \dots, n) \tag{7}$$

where LB_{X_i} and UB_{X_i} are the upper and lower bounds of the design variable x_i. The boundary can be represented by $g_{bou}(X)$. The magnitudes of these boundary variables are determined subjected to both manufacturing and part geometry constraints.

5.2 Area Constraints

The strain energy caused by the external loads is inversely proportional to the area of the cross section of a fixed length structure [58, 59]. Minimising the strain energy of the channel by changing the geometrical parameters will change the weight of the structure. Therefore, it is important to include a constraint on the maximum weight of the part. Here, the whole structure is built from a constant thickness pre-cut blank with single isotropic material. As the manufacturing process is a variant of roll forming, the thickness of the formed channel is assumed to be uniform and unchanged compared with the pre-cut blank during the entire
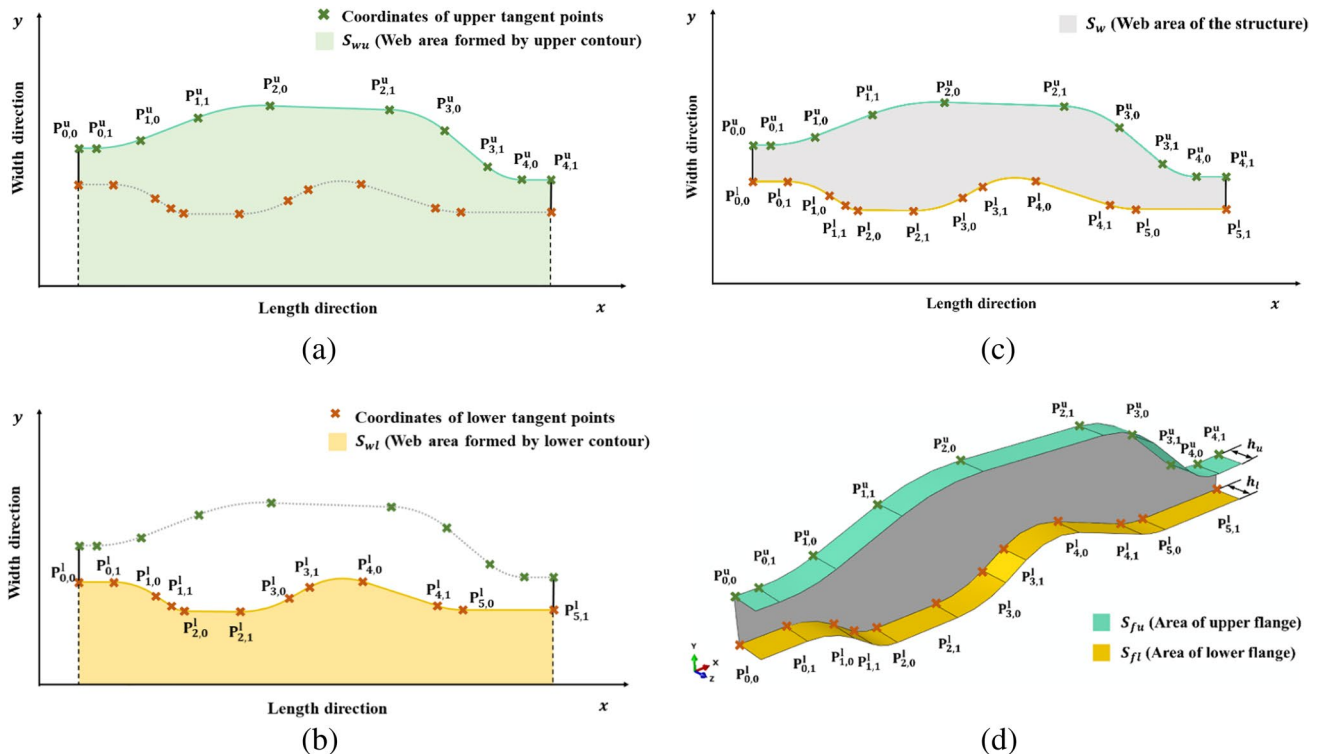

Fig. 6 Method of calculating the area of the structure, (a). Web area formed by the upper contour, (b). Web area formed by lower contour, (c). Web area, (d). Flange areas formed by upper and lower contours
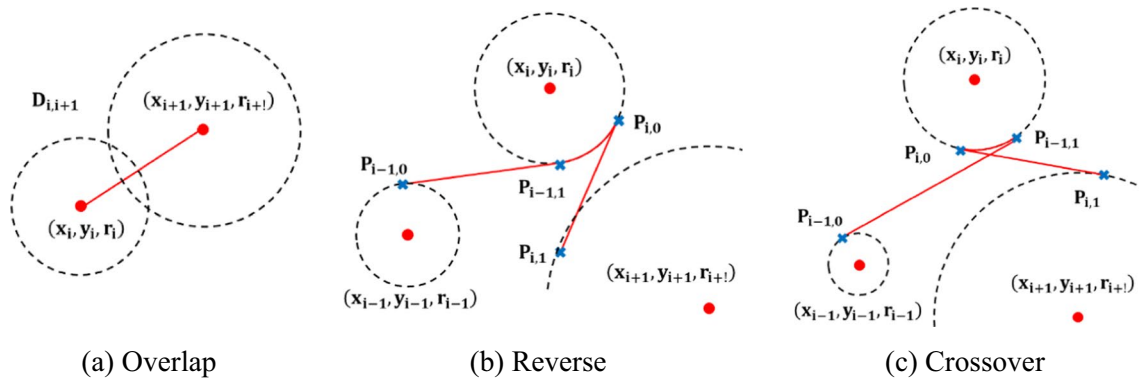
Fig. 7 Geometrical constraints based on the developed modelling method

optimisation process. Therefore, the weight constraint can be represented by the surface area of the formed channel. The total area of the channel is defined as:

$$S(X) = S_{wu}(X) - S_{wl}(X) + S_{fu}(X) + S_{fl}(X) \tag{8}$$

where $S_{wu}(X)$ (Fig. 6(a)) and $S_{wl}(X)$ (Fig. 6(b)) are the web areas of the upper and lower profiles positioned above the x-axis, respectively. The overlapping area of $S_{wu}(X)$ and $S_{wl}(X)$ is the total web area of the channel (Fig. 6(c)). $S_{fu}(X)$ and $S_{fl}(X)$ are the areas of the upper and lower flanges, which can be obtained based on the length of the upper and lower profiles (Fig. 6(d)).

Calculating the profile of the structure can be divided into straight and transitional sections while the area of the web (Fig. 6 (c)) and flanges (Fig. 6 (d)) can be represented with the points of tangency ($P_{i,j}(X_{i,j}, Y_{i,j})$) (full formulation presented in Appendix B). The area constraint is expressed as:

$$g_s(X) = S(X) - S(X_{initial}) \leq 0 \tag{9}$$

The integrated area constraint ensures that the weight of the channel is not increased during the optimisation process.

5.3 Geometrical Constraints

Given the flexibility of the parametric method, in some cases, impossible geometrical combinations of shape configurations may occur, which results in invalid shape modes. Therefore, all possible ill-conditioned relationships were identified and formulated into the optimisation platform as geometrical constraints. There are three kinds of geometrical constraints: overlap between two arcs, reverse direction, and crossover between two straight sections, as shown in Fig. 7.

As the parametric model forms channels based on the calculated points of tangency $P_{i,j}(X_{i,j}, Y_{i,j})$ ($j = 0, 1$) (Figs. 4

Fig. 8 Relation between design variables and points of tangency
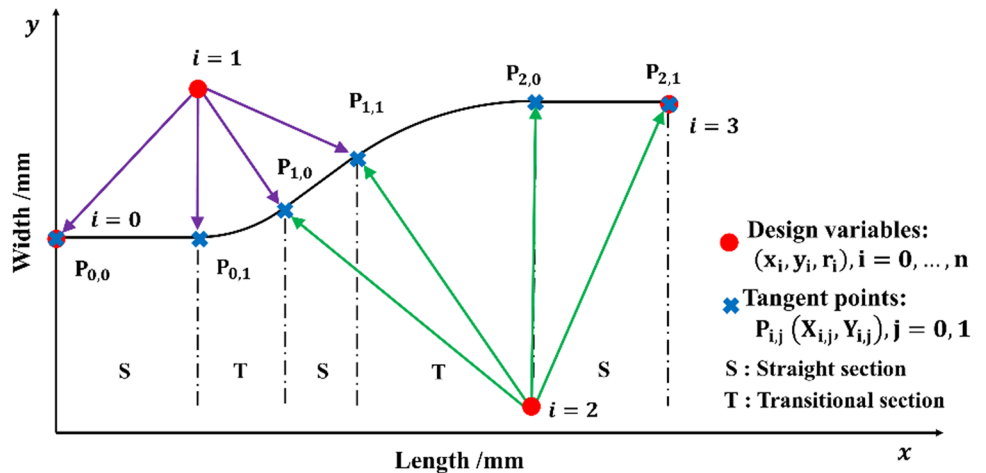
and 7), the geometrical constraints can be formulated based on these points which in turn are dependent on the design variables.

When the distance between the centres of the two arcs is shorter than the sum value of the radii of these two arcs, the overlap will be generated (Fig. 7(a)). This situation needs to be avoided by adding the following constraint:

$$g_{olp}(X) = |r_i| + |r_{i+1}| - D_{i,i+1} \leq 0 \ (i = 0, \ldots, n) \tag{10}$$

where r_i and r_{i+1} are the radii of the adjacent arcs, and $D_{i,i+1}$ is the distance between them.

Based on the definition of the reverse (Fig. 7(b)) and the crossover conditions (Fig. 7(c)), these two constraints can be formulated as described in Eqs. (11) and (12),

$$g_{rev}(X) = X_{i,0} - X_{i,1} \leq 0 \quad (i = 0, \ldots, n) \tag{11}$$

$$g_{cro}(X) = X_{i-1,1} - X_{i,0} \leq 0 \quad (i = 1, \ldots, n) \tag{12}$$

Denoting $g_c(X) = [g_s(X), \ g_{bou}(X), \ g_{ten}(X), \ g_{com}(X), \ g_{olp}(X), \ g_{rev}(X), g_{cro}(X) \ ]^T$ and $\in R^n$, the shape optimisation problem can be stated as:

$$\left. \begin{array}{l} \min \ f(X) \\ \text{subject to} \quad g_c(X) \end{array} \right\} \tag{13}$$

5.4 Sensitivity Analysis

The challenge in gradient-based optimisation is the sensitivity analysis that determines the optimisation direction [60, 61]. Here, first order derivatives of the objective and constraints with respect to design variables are derived with numerical and analytical methods.
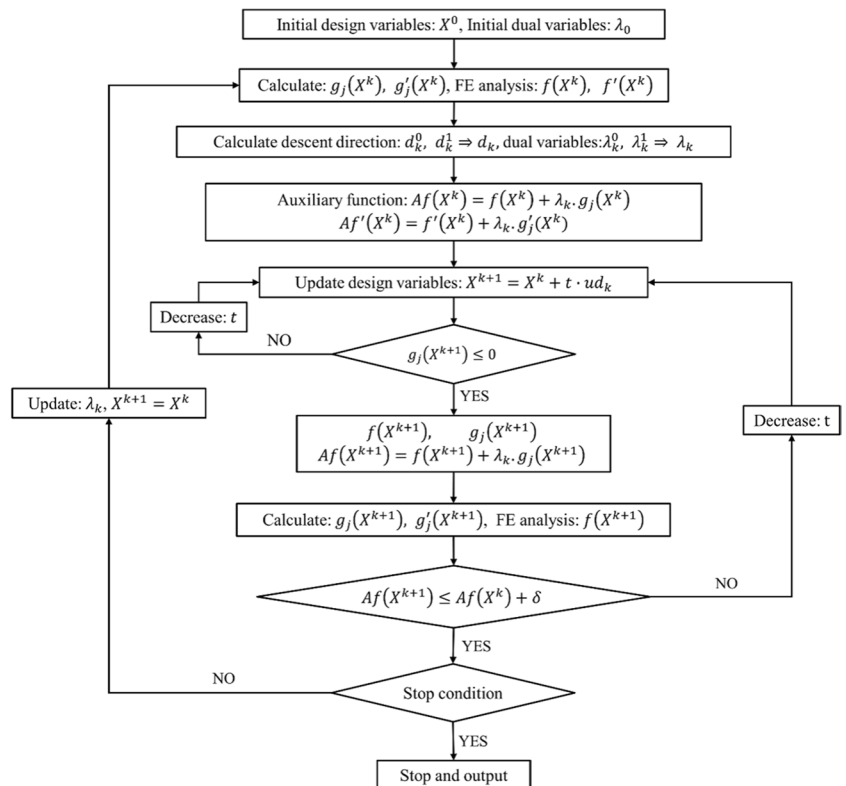
5.4.1 Sensitivity Analysis of the Objective Function

The finite difference technique is an easy way to calculate the sensitivity of the objective function with no need of coding or formulating equations. However, this method might be calculation intensive for the problem requiring numerous design parameters. This drawback can be avoided in this work, because only a small number of design variables are needed to form the complicated structure based on the proposed parametric method in Section 2. Therefore, the finite difference technique is used to approximate the sensitivity of the objective function, which is stated as:

$$\frac{\partial f(X)}{\partial X} = \lim_{\Delta X \to 0} \frac{f(X^{k+1}) - f(X^k)}{\Delta X} \tag{14}$$

where $\Delta X = td = X^{k+1} - X^k$, ΔX stands for the vector of the design perturbation determined by step size t and descent direction d. The step size and descent direction can be calculated and updated by the optimiser during the optimisation

Fig. 9 Flowchart of the optimisation procedure

process. X^{k+1} and X^k are the vectors of design variables corresponding to the objective function $f(X^{k+1})$ and $f(X^k)$, respectively. As X is a vector of the design variables, the sensitivity of the objective function can be formulated as:

$$\nabla f(X) = \left[\frac{\partial f(X)}{\partial x_0}, \ldots, \frac{\partial f(X)}{\partial x_n} \right] \tag{15}$$

5.4.2 Sensitivity Analysis of the Constraints

The sensitivity analysis of the area constraints can be developed based on Eq. (8) as:

$$\frac{\partial g_s(X)}{\partial X} = \frac{\partial S_{wu}(X)}{\partial X} - \frac{\partial S_{wl}(X)}{\partial X} + \frac{\partial S_{fu}(X)}{\partial X} + \frac{\partial S_{fl}(X)}{\partial X} \tag{16}$$

However, differentiating Eq. (16) with respect to the design variables requires the analysis of the points of tangency that are intermediate variables ($P_{i,j}(X_{i,j}, Y_{i,j})$). The relationship between the design variables and intermediate variables in the modelling method is illustrated in Fig. 8, where the change of one design variable affects four intermediate variables (points of tangency).

Therefore, the sensitivity of the area with respect to one design variable can be expressed as:

$$\frac{\partial g_s(X)}{\partial x_i} = \begin{cases} \sum_{j=0}^{1} \frac{\partial S(X)}{\partial P_{i,j}} \frac{\partial P_{i,j}}{\partial x_i} & (i = 0) \\ \sum_{j=0}^{1} \left(\frac{\partial S(X)}{\partial P_{i-1,j}} \frac{\partial P_{i-1,j}}{\partial x_i} + \frac{\partial S(X)}{\partial P_{i,j}} \frac{\partial P_{i,j}}{\partial x_i} \right) & (i = 1, \ldots, n-1) \end{cases} \tag{17}$$

where $\frac{\partial S(X)}{\partial P_{i,j}} = \frac{\partial S_{wu}(X)}{\partial P_{i,j}} - \frac{\partial S_{wl}(X)}{\partial P_{i,j}} + \frac{\partial S_{fu}(X)}{\partial P_{i,j}} + \frac{\partial S_{fl}(X)}{\partial P_{i,j}}$ and $\frac{\partial P_{i,j}}{\partial x_i}$ can be obtained according to the formulation presented in Appendix A.

The derivative of the area with respect to the design variables is expressed as:

Table 1 Material properties of DP780 steel [66]

Mass density (kg/m^3)	Young's modulus (GPa)	Poisson's ratio	Yield stress (MPa)	Ultimate stress (MPa)
7850	200	0.3	597	960

$$\frac{\partial g_s(X)}{\partial X} = \left[\frac{\partial g_s(X)}{\partial x_0}, \ldots, \frac{\partial g_s(X)}{\partial x_n} \right]^T \tag{18}$$

The sensitivity analysis of other constraints including boundaries (Eqs. (3), (4) and (7)) and geometries (Eqs. (10), (11) and (12)) can be derived based on the formulation presented in Appendix A.

The sensitivity analyses of constraints can be summarised as:

$$\nabla g_c(X) = \left[\frac{\partial g_s(X)}{\partial x_i}, \frac{\partial g_{bou}(X)}{\partial x_i}, \frac{\partial g_{olp}(X)}{\partial x_i}, \frac{\partial g_{rev}(X)}{\partial x_i}, \frac{\partial g_{cro}(X)}{\partial x_i} \right]^T (i = 0, \ldots, n) \tag{19}$$

After the formulation of the problem and the sensitivity analysis, the optimisation model in Eq. (13) can be solved by gradient-based optimisers.

6 Optimisation Algorithm

This paper adopts the modified Newton-like algorithm proposed by Herskovits [62] as the optimiser to update the design variables iteratively. The method is efficient and robust in solving large-scale nonlinear and linear programming compared to widely used GA [37]. An initial estimate of the design variables that are in the feasible domain defined by the constraints is required for the initiation of the optimisation. The Lagrangian function is introduced:
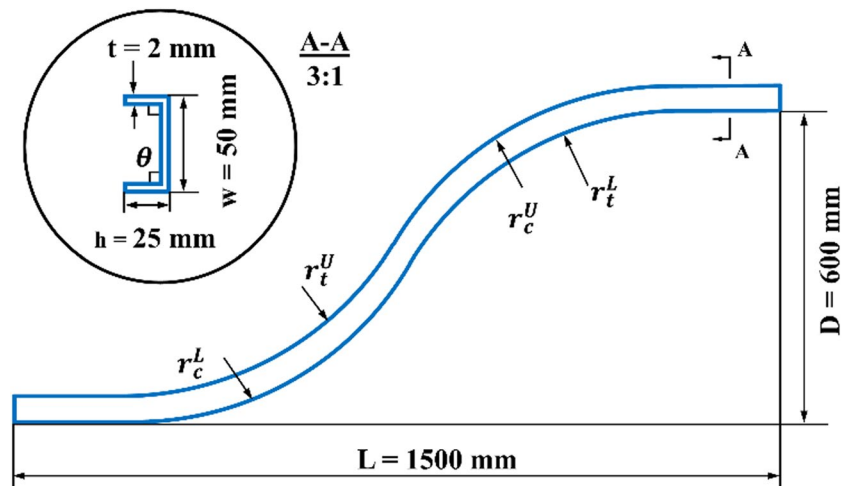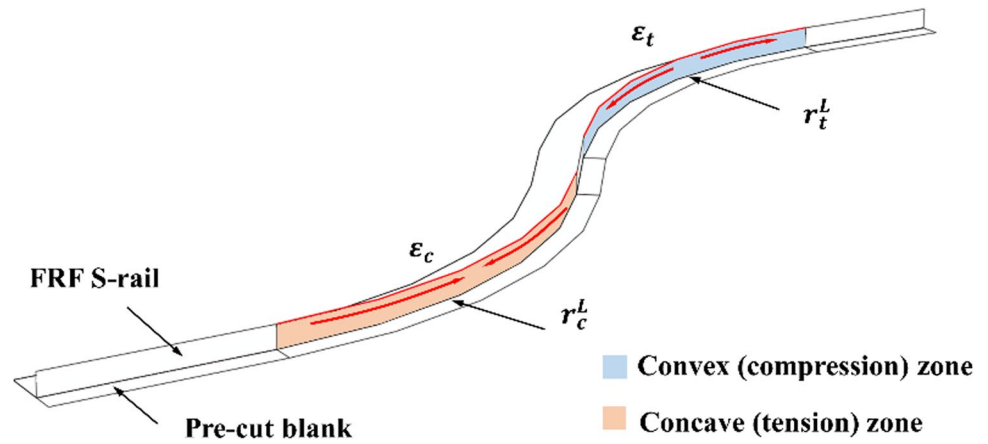
Fig. 10 Geometric parameters of the simplified S-rail

Fig. 11 Schematic of the half S-rail with the strain limit in critical regions

$$\mathcal{L}(X, \lambda) = f(X) - \lambda^t g_c(X) \qquad (20)$$

where $\lambda \in R^m$ gives the dual variables. The Karush-Kuhn-Tucker first order necessary conditions [37] stated below are utilised to explore a feasible direction with respect to the objective and constraints:

$$\nabla \mathcal{L}(X^*, \lambda^*) = 0 \qquad (21)$$

$$G(X^*)\, \lambda^* = 0 \qquad (22)$$

$$\lambda^* = 0 \qquad (23)$$

$$g_c(X^*) \le 0 \qquad (24)$$

where $G(X^*)$ is a diagonal matrix and the elements of main diagonal are $g_c(X^*)$. After each iteration, a new vector of X^* will be obtained and the structural configuration is updated based on it.

An FEA model is constructed to assess the performance of optimised structures subjected to specified loading conditions. The commercial FEA software ABAQUS 2020 is used as the solver. The parametric model, optimisation algorithm and FEA model are combined to form the optimisation platform using a built-in ABAQUS Python script. The optimisation process of the proposed methodology is shown in Fig. 9.

The auxiliary function shown in Fig. 9 is used as the termination criterion in the Armijo's Line Search to determine the step size at each iteration. The proposed parameterisation technique forms the structural configuration based on the design variables in the design domain. Then, these parameters are transferred into FEA. The result of FEA allows the objective function to be calculated and written into the output file. The platform compares the results according to the auxiliary function and convergence criteria. New design variables that reduce the objective function and satisfy all constraints are chosen as inputs in the next iteration. There are two termination criteria, the maximum number of iterations and the ratio of change in the auxiliary function. The ratio of change in the auxiliary function is defined as:

$$\epsilon = \frac{\left| Af\left(X^{k+1}\right) - Af\left(X^k\right) \right|}{\left| Af\left(X^{k+1}\right) \right|} \le \tau \qquad (25)$$

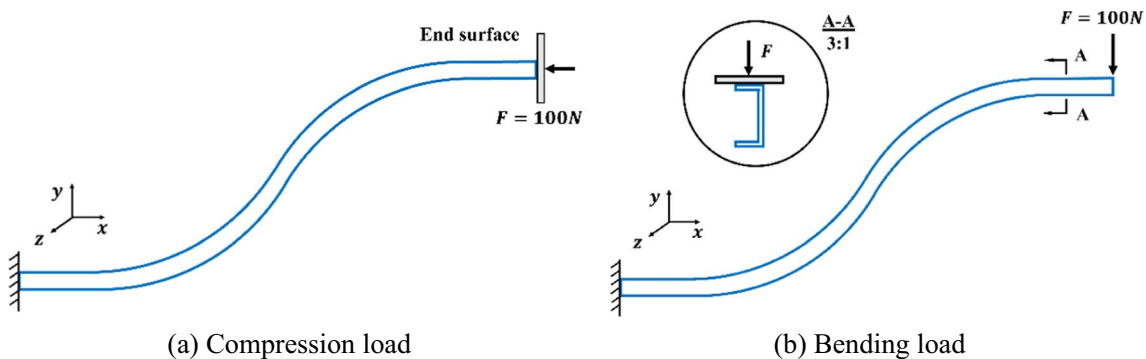(a) Compression load   (b) Bending load

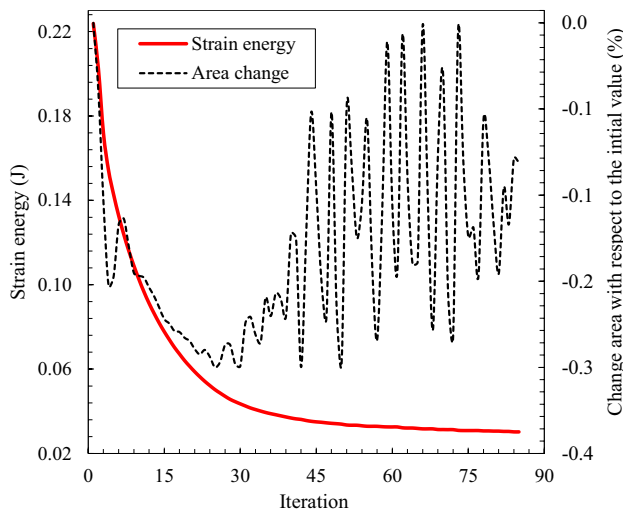**Fig. 12** The two loading conditions analysed in the S-rail optimisation problems

Fig. 13 Convergence process of the objective and the change of the area for Case 1

where τ is an allowable tolerance and $Af(X^k)$ is the value of the auxiliary function in the k_{th} iteration. If the convergence criteria are met, the optimisation process terminates, and the result is an improved configuration.

7 Case Studies

S-rails situated in the front and rear sides of the automotive body in white play a vital role in preventing drivers from being severely injured in crash events by absorbing the impact energy [63]. Current S-rails are commonly stamped [64], however FRF presents a more flexible and

cost-effective alternative [56]. To investigate the S-rail, the shape is simplified as shown in Fig. 10 and modelled by the proposed parametrisation method in Section 2. Numerical experiments are then applied to the S-rails to validate the flexibility and robustness of the proposed optimisation platform via three case studies.

The geometric dimensions of the initial S-rail design are shown in Fig. 10, where *L*, *D*, *w*, *h*, *t* and θ represent the total length of the S-rail, the offset of the two-end parts, the left and right ends of the web width, the flange height, the wall thickness and the bend angle between the web and the flange, respectively. r_t^U, r_c^U, r_t^L and r_c^L are the radii of the upper concave (tension) flange section, the upper convex (compression) flange section, the lower concave (tension) flange section, and the lower convex (compression) flange section, respectively. Here, the values of *L*, *D*, *W*, *h*, *t* and θ are based on [65] and have been fixed as shown in Fig. 10.

The S-rail is modelled in ABAQUS Implicit as a deformable part using four node shell elements (S4R) with 5 integration points (through-the-thickness). It is assumed that the material of the S-rail is an isotropic DP 780 steel. The material properties used for optimisation are listed in Table 1.

As previously mentioned, excessive longitudinal strain generated along the flange will lead to web warping or wrinkling. The critical regions in the S-rail with the corresponding maximum longitudinal strain for tension and compression are shown in Fig. 11. To avoid the initiation of defects, the manufacturing constraints outlined in Eqs. (3) and (4) are considered in the optimisation process. Here, the approximate strain limits for compression ($\hat{\varepsilon}_c$) and tension ($\hat{\varepsilon}_t$) for high DP 780 steel with a thickness of 2 mm are $\varepsilon_c = -0.04$ and $\varepsilon_s = 0.2$ [42]. As the height of the flange (*h*) and the bend angle (θ) are fixed

Table 2 Comparison between the results of the initial and the optimised structure for Case 1

Iteration	Upper design variables (mm)						Lower design variables (mm)						Performance	
	xu1	xu2	yu1	yu2	ru1	ru2	xl1	xl2	yl1	yl2	rl1	rl2	Strain energy (J)	Area(mm²)
Initial	215.00	1285.00	870.00	230.00	-620.00	620.00	240.00	1310.00	820.00	180.00	-620.00	620.00	0.22	175492.30
Optimised	198.67	1290.29	909.71	158.39	-573.80	645.48	198.81	1329.42	868.43	193.34	-634.06	608.59	0.03	175292.47
Change (Δ)	-16.33	5.29	39.71	-71.61	46.20	25.48	-41.19	19.42	48.43	13.34	-14.06	-11.41	-0.19	-199.83
Change ratio	-7.60%	0.41%	4.56%	-31.13%	-7.45%	4.11%	-17.16%	1.48%	5.91%	7.41%	2.27%	-1.84%	-86.49%	-0.11%

Initial design	Optimised design
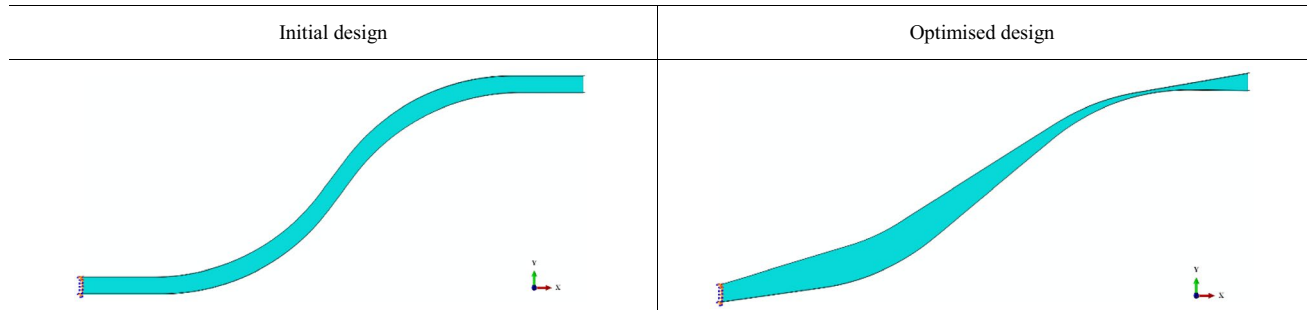
(Fig. 10), the minimum radii of the concave and the convex zones in the S-rail can be calculated based on Eqs. (3) and (4), obtaining r_c^{min} = 612.95 mm and r_t^{min}=137.92 mm. These lower limits of radii are defined as manufacturing constraints in the optimisation platform to avoid any defect initiation during part manufacture with FRF. The optimisation process only focusses on the linear behaviour of the material.

As the major purpose of the S-rail is to resist the front and side crash, the stiffness of the structure is one important aspect for the evaluation of the structural performance. In the cases solved here, six degrees of freedom are constrained on one end of the S-rail, while the other end is loaded by either compression or bending, as shown in Fig. 12. The objective function of the optimisation is to minimise the strain energy or to maximise the stiffness of the S-rail on condition that the total weight does not increase.

7.1 S-rail Subjected to Compression Load

7.1.1 Case 1: Four Sets of Design Variables

In the first numerical example, the initial S-rail is optimised under a compression load applied on the right end surface, as demonstrated in Fig. 12(a). Twelve design variables, which form the upper and lower transitional sections, are selected as shown in Fig. 4 (*i* equals to 1 and 2). The upper and lower bounds of these design variables can be calculated based on the given parameters (Fig. 10) and manufacturing constraints (Eqs. (3) and (4)).

The optimisation results of the objective function (strain energy) are shown in Fig. 13 and indicate an 86.49% decrease from 0.22 J to 0.03 J. The solution converged at the 85th iteration after reaching the termination criterion (Eq. (25)). Compared with the initial design, the optimised S-rail yields a minimal 0.11% area reduction. The dynamic view of the S-rail and the change of the design variables are demonstrated in Table 2.

An obvious decrease in rail deformation is observed when comparing the initial and the optimised S-rails shown in Fig. 14(a) and (b) respectively. The magnitude of the maximum displacement reduces from 26.96 mm to 2.80 mm, meaning that the optimised structure is almost 90% stiffer than the original one. This verifies the change of the objective function shown in Fig. 13. In addition, the maximum stress in the optimised structure is 54.69% less than that in the original one (Fig. 14(c) and (d)).

7.2 S-rail Subjected to Bending Load

7.2.1 Case 2: Four Sets of Design Variables

The same design variables and geometric properties as used for Case 1 are applied in Case 2. The S-rail is now subjected to a bending force in the negative y-direction (Fig. 12(b))

and the convergence history is shown in Fig. 15. The optimised structure that is obtained at the 58th iteration shows a 51.62% reduction from 0.88 J to 0.42 J in the strain energy and a 0.09% reduction in area compared to the initial design. Table 3 displays the effect of the design variables change on the shape of the S-rail after the optimisation process. The displacement decreases from 46.92 mm to 11.77 mm compared to the initial S-rail shown in Fig. 16 (a) and (b) i.e., the optimised structure is about 74.91% stiffer than the initial design. A 10.13% reduction of the maximum stress can also be observed when comparing the initial and the optimised S-rail in Fig. 16(c) and (d), respectively.
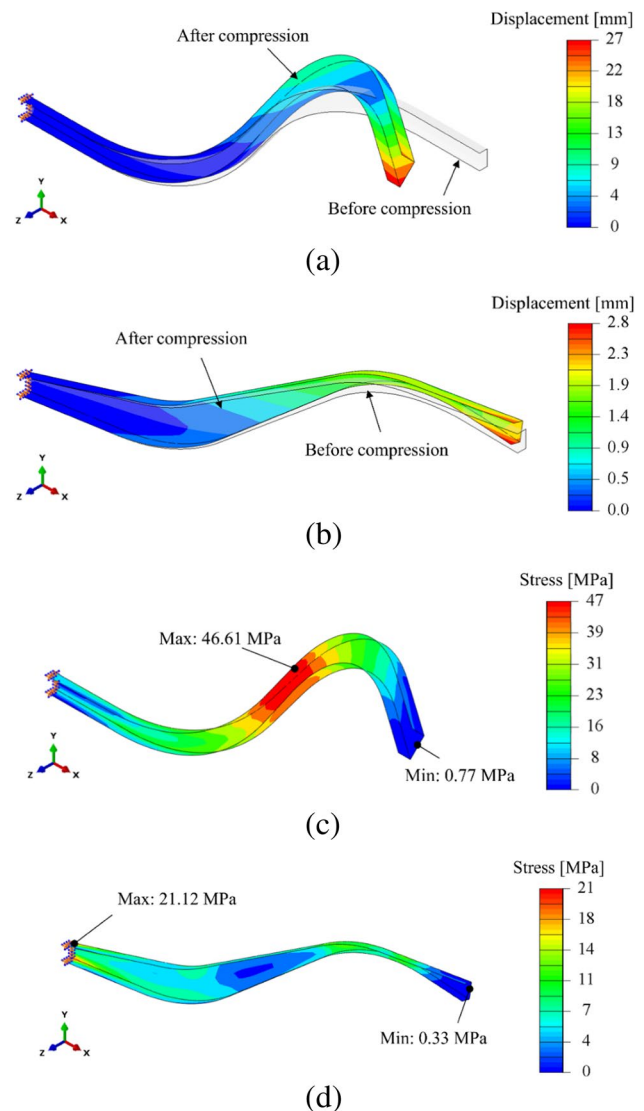

Fig. 14 Contour plots of displacement and stress for the S-rail under compression before and after optimisation for Case 1, (a) the displacement of the initial S-rail before and after compression, (b) the displacement of the optimised S-rail before and after compression, (c) the initial S-rail after compression, (d) the optimised S-rail after compression
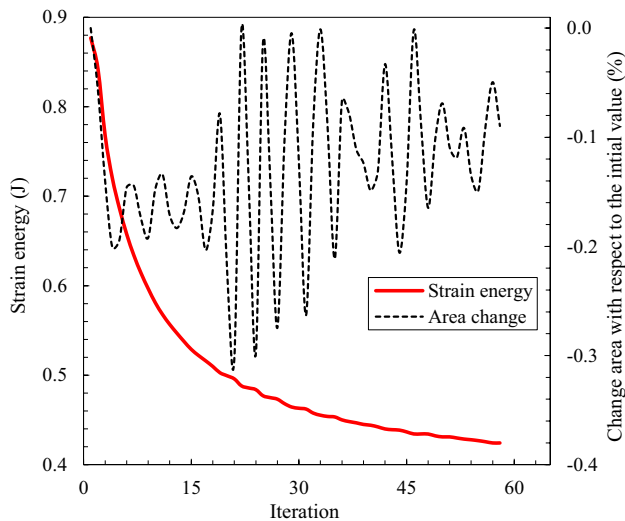
Fig. 15 Convergence process of the objective and the change of the area for Case 2

7.2.2 Case 3: Four Sets with an Additional Design Variable

In Cases 1 and 2, all the design variables are in triplet format (x_i, y_i, r_i). Therefore, an additional single design variable yu_0 shown in Fig. 4 (i equals to 0) is introduced here to test the capability of the modelling method to handle different forms of design variables. The initial structure and load condition as used for Case 2 were applied here. The convergence process is shown in Fig. 17. The optimised structure of Case 3 achieves a 64.58% strain energy reduction combined with a slightly lighter weight after the 73rd

iteration. It is clear that a further strain energy reduction (0.11 J) has been obtained in Case 3 (red line) compared to Case 2 (purple line). Yet the area of the optimised results in Case 3 (175486.85 mm^2) is slightly larger than that in Case 2 (175334.86 mm^2). The changes of shape configurations before and after optimisation are shown in Table 4. Comparing the maximum displacement of the initial and optimised S-rail in Fig. 18 (a) and (b) respectively, the stiffness improved by 84.31% while the maximum stress decreased from 91.02 MPa to 48.06 MPa (47.30% reduction) (see Fig. 18 (c) and (d)). In contrast to this, the structure optimised in Case 2 only shows a stiffness increase of 74.91% and a 10.13% reduction of the maximum stress (Fig. 16).

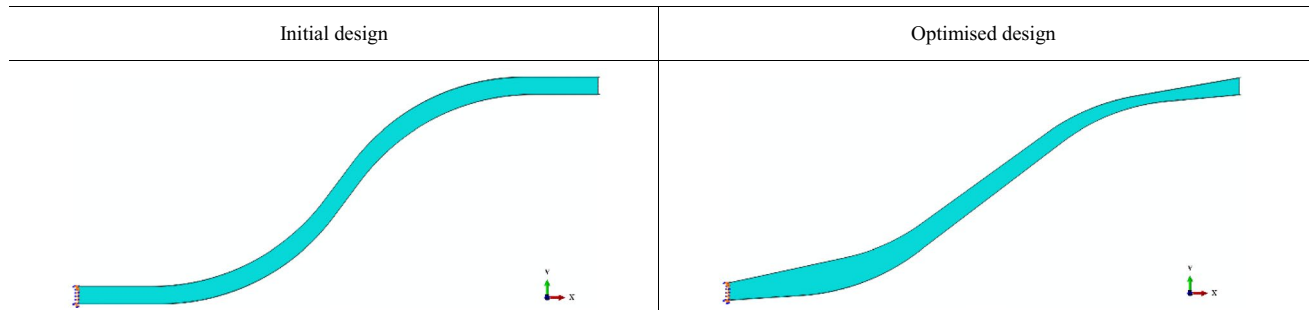## 8 Manufacturing Simulation of the Optimised Structure

This section presents the simulation results of the FRF process for the optimised S-rail structure to show the manufacturing feasibility of the structure and to proof the structural performance by considering the residual stresses introduced by the manufacturing process. The structure optimised for the bending load in Case 3 is selected for the manufacturing simulation. For testing the manufacturing feasibility, two FEA models are created in Abaqus.

8.1 Static Implicit Model for Forming the Critical Regions of the Flange

The first model is a static implicit model that is based on a previous study [67] and has been validated by experimental shape and strain measurements. As mentioned earlier, flange wrinkling

Table 3 Comparison between the results of the initial and the optimised structure for Case 2

Iteration	Upper design variables (mm)						Lower design variables (mm)						Performance	
	xu1	xu2	yu1	yu2	ru1	ru2	xl1	xl2	yl1	yl2	rl1	rl2	Strain energy (J)	Area(mm^2)
Initial	215.00	1285.00	870.00	230.00	-620.00	620.00	240.00	1310.00	820.00	180.00	-620.00	620.00	0.88	175492.30
Optimised	220.08	1300.68	903.47	171.27	-592.08	634.29	173.86	1341.28	847.94	182.77	-635.72	600.35	0.42	175334.86
Change (Δ)	5.08	15.68	33.47	-58.73	27.92	14.29	-66.14	31.28	27.94	2.77	-15.72	-19.65	-0.45	-157.44
Change ratio	2.36%	1.22%	3.85%	-25.53%	-4.50%	2.31%	-27.56%	2.39%	3.41%	1.54%	2.54%	-3.17%	-51.62%	-0.09%

Initial design	Optimised design

Fig. 17 Convergence process of the objective and the change of the area for Case 3
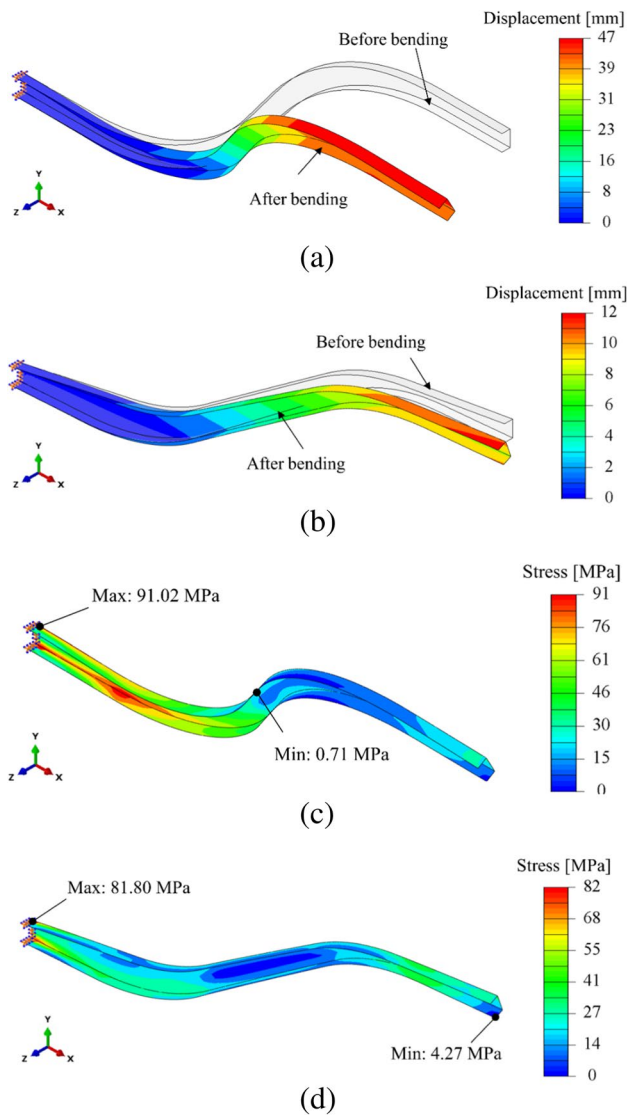
Fig. 16 Contour plots of displacement and stress for the S-rail under bending load before and after optimisation for Case 2, (a) the displacement of the initial S-rail before and after bending load, (b) the displacement of the optimised S-rail before and after bending load, (c) the initial S-rail after bending load, (d) the optimised S-rail after bending load

is the major challenge for FRF. Therefore, the static analysis is limited to the two convex regions (as highlighted in Fig. 19) where the flange is under longitudinal compression and is likely to show wrinkling. This saves the computational effort as running an implicit analysis of the full component would require more than 30,000 elements and is very time consuming.

The key model features such as the part type, the blank and die element types, material definition, contact properties, damping factor and boundary conditions for the tool movements are the same as used in the previous study [67]. The bending sequence used for the forming simulation of both regions is shown in Fig. 20 (a). Each forming pass is
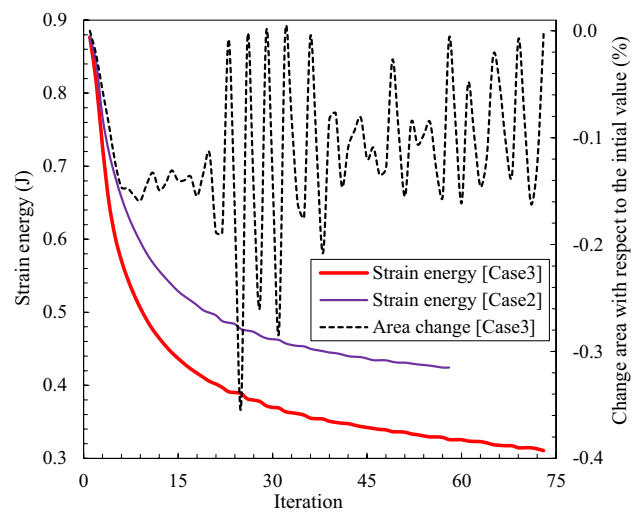
modelled as one single implicit step with a time period of 11.2 seconds. The cross-section of the forming roll is shown in Fig. 20(b). A 2mm thick DP780 material is used for modelling the process, and the properties are given in Table 1.

A bending radius of 4mm is selected (Fig. 20 (a)) to minimise springback as well as to keep the element size optimum at 0.6mm in the bending zone as shown in Fig. 21. The element size along the longitudinal direction is fixed at 3.4 mm. The blank is fixed along the transverse (Z) and the longitudinal (X) direction for both regions as shown in Fig. 21 (a) and (b).

### 8.1.1 Shape and Strain Measurements from the Simulation Output

The shape and strain measurements from the FEA models are analysed along the node paths (as shown in Fig. 22) to determine the deviation in the shape of the formed blank from the ideal CAD design. This provides an indication of the feasibility of manufacturing the part shape. The deformed mesh after the final forming pass is plotted in Fig. 22 for the two critical convex regions along with the ideal CAD profile. The average shape deviations (δ_{xz}) of the flange edge are calculated along the X (length) and the Z (width) direction according to the formula:

$$\delta_{xz} = \frac{1}{n} \sum_{x=1}^{x=n} |Z_{x-FEA} - Z_{x-CAD}| \tag{26}$$

where Z_{x-FEA} and Z_{x-CAD} are the Z-X coordinate points of the flange edge from the FEA and the CAD, respectively while n is the number of nodes in the node path. The δ_{xz} for

Table 4 Comparison between the results of the initial and the optimised structure for Case 3

Iteration	Upper design variables (mm)							Lower design variables (mm)						Performance	
	xu1	xu2	yu0	yu1	yu2	ru1	ru2	xl1	xl2	yl1	yl2	rl1	rl2	Strain energy (J)	Area(mm²)
Initial	215.00	1285.00	250.00	870.00	230.00	-620.00	620.00	240.00	1310.00	820.00	180.00	-620.00	620.00	0.88	175492.30
Optimised	213.54	1301.60	296.35	916.20	165.66	-584.64	634.28	193.35	1344.04	881.27	178.92	-630.20	600.84	0.31	175486.85
Change (Δ)	-1.46	16.60	46.35	46.20	-64.34	35.36	14.28	-46.65	34.04	61.27	-1.08	-10.20	-19.16	-0.57	-5.46
Change ratio	-0.68%	1.29%	18.54%	5.31%	-27.97%	-5.70%	2.30%	-19.44%	2.60%	7.47%	-0.60%	1.64%	-3.09%	-64.58%	-0.003%

Initial design	Optimised design
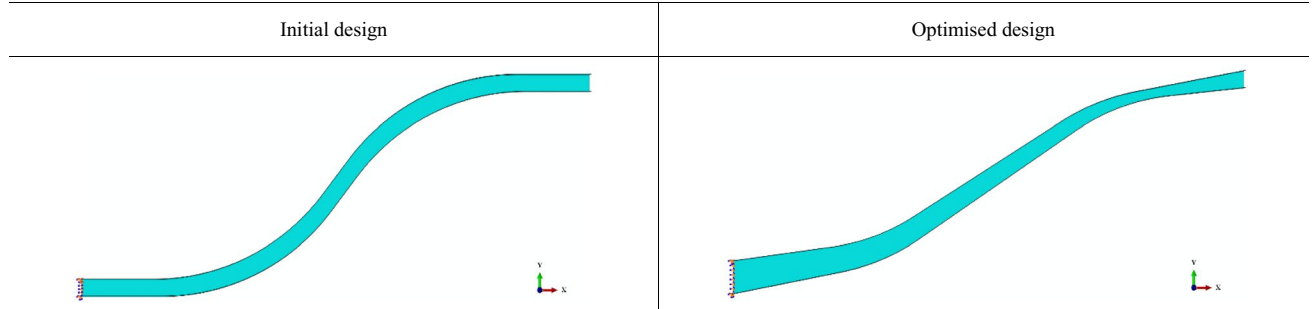
the convex regions-1 and 2 are calculated to be 0.55 mm and 0.59 mm, respectively.

The springback measurements are carried slicing three planes across the cross section of the formed component as shown in Fig. 23. The average springback values are calculated to be 1.33° and 2.96° for convex regions- 1 and 2, respectively.

The minimum principal strain component along the flange edge (at the middle integration point) is plotted in Fig. 24 (a) and (b) to show the level of compressive deformation achieved in the flange after each forming pass. To compare the strains, the analytical strain value is calculated from Eq. (2) and compared to the FEA strain distribution. The FEA shows that a smooth uniform distribution of strain is achieved after each pass for both convex regions. The peak compressive strain values achieved after each pass are close to the analytical values for most forming passes in both regions. There is only a small deviation in passes 5 and 6 in region-1 and passes 4,5 and 6 in region-2. This could be either related to springback or due to the limitations of the analytical equations in predicting the exact strain value [67]. Regardless of this, it can be concluded that the strain distribution from the FEA shows a good forming of the flange without any major wrinkling defects. This provides the initial confirmation that the optimised part is manufacturable according to an experimentally validated process simulation model of FRF.

8.2 FEA Model for Forming the Full Structure

A dynamic explicit model is used to simulate the forming process for the full structure, for running the forming simulation of a full S-rail structure with mass scaling to speed up the simulation. This model is used to create a final stress state of the formed component, which can be imported to the structural testing model of the S-rail component in Section 7.2. The model parameters such as the part, mesh type, tool and blank boundary definitions are kept the same as those in the implicit model. The bending sequence and roll tools are also the same as shown in Fig. 20. The key changes that were introduced are:

- The forming steps are changed to the dynamic explicit type with a total step time of 352.8 seconds.
- The blank material is defined with a density of 7750 Kg/m³.
- Mass scaling of the blank is introduced to achieve a fixed time increment of 0.001 seconds.
- The contact algorithm is changed to surface-to-surface explicit.

The analysis is performed in three steps. In the first step, the full forming simulation is performed using the explicit analysis to extract the final stress state of the formed part. In the second step, the model performs a static implicit analysis for the unclamping operation where the blank is released from the die and the boundary conditions are removed. In the final step, the released implicit model with the extracted stresses is subject to the same loading condition in Case 3 to validate the structural performance of the optimised component.

8.2.1 Deformed State after Forming and Unclamping

The deformed shape with the stress contour on the blank after the forming simulation using the explicit analysis is shown in Fig. 25 (a). The Mises stress and the minimum principal strain
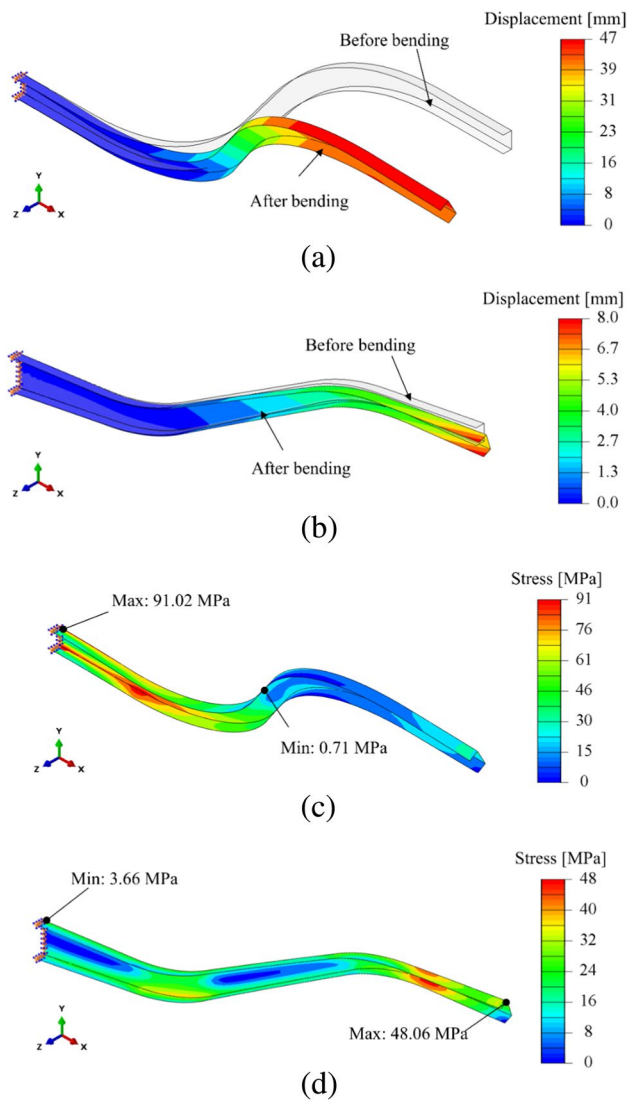
Fig. 18 Contour plots of displacement and stress for the S-rail under bending load before and after optimisation for Case 3, (a) the displacement of the initial S-rail before and after bending load, (b) the displacement of the optimised S-rail before and after bending load, (c) the initial S-rail after bending load, (d) the optimised S-rail after bending load

Fig. 19 Convex regions of the optimised structure which may show to flange wrinkling
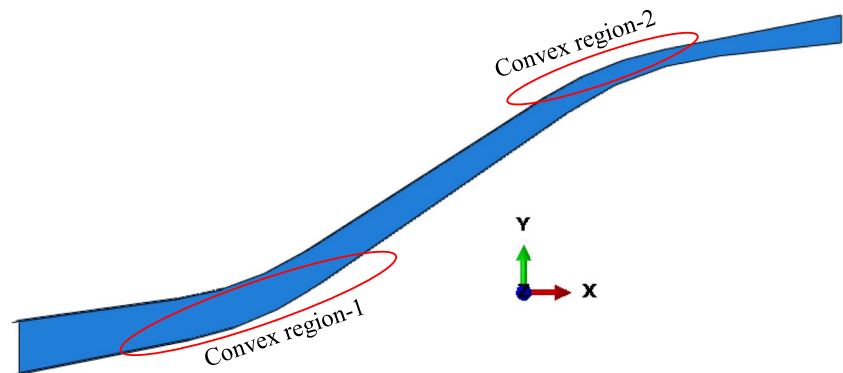
along the flange edge are compared between the two implicit models in Section 8.1 (Fig. 21) and the corresponding regions in the explicit model for assessing the accuracy of the explicit analysis. The stress and strain extracted from the node paths after final forming pass are shown in Fig. 25.

The comparison shows that the strain and stress values from explicit analysis are slightly lower than those of the implicit analysis. Overall, there is a good correlation. In addition to this, the ratio of kinetic energy to internal energy is below 5% throughout the entire forming in the explicit analysis, which suggests that the inertia effect is negligible.

The deformed shapes before and after unclamping the formed blank component are shown in Fig. 26 (b). It can be noticed that the formed component shows some twisting after the unclamping operation. This means that the formed structure may have some defects in the form of longitudinal twist, and this needs to be considered.

8.2.2 Structural Testing of Unclamped Component

The structural testing of the unclamped shape is carried out using the static implicit analysis with only elastic material considerations presented in Section 7.2. Since the application of the concentrated load causes convergence issues due to the presence of residual stresses, the bending load is applied at the end using contact with rigid shell punch as shown in Fig. 27. In this case, a simple displacement in the vertical direction is applied with a static implicit step using a punch with a time period of 1 second. This is applied to both the original model without the forming stresses and the model with residual stress imported from the manufacturing simulation.

The structural test does not enable a comparison and the analysis of the effect of residual stress on the structural load. Given that the component with the residual forming stresses is twisted. It does not reflect on the same manner as component without residual stress. This is illustrated in Fig. 28. The original model shows that the deflected shape stays within the ZX plane, i.e., the load is pure bending. However, the twisted shape with forming stresses shows that the deflection tends to move out of the ZX plane which gives
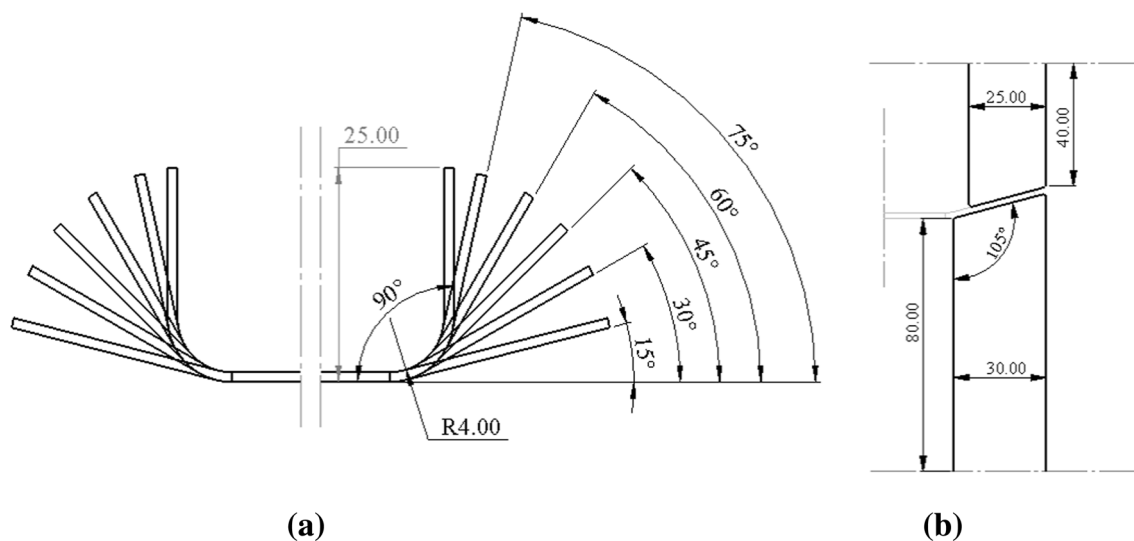
Fig. 20 (a) Bending sequence for FRF simulation; (b) Cross section of forming rolls
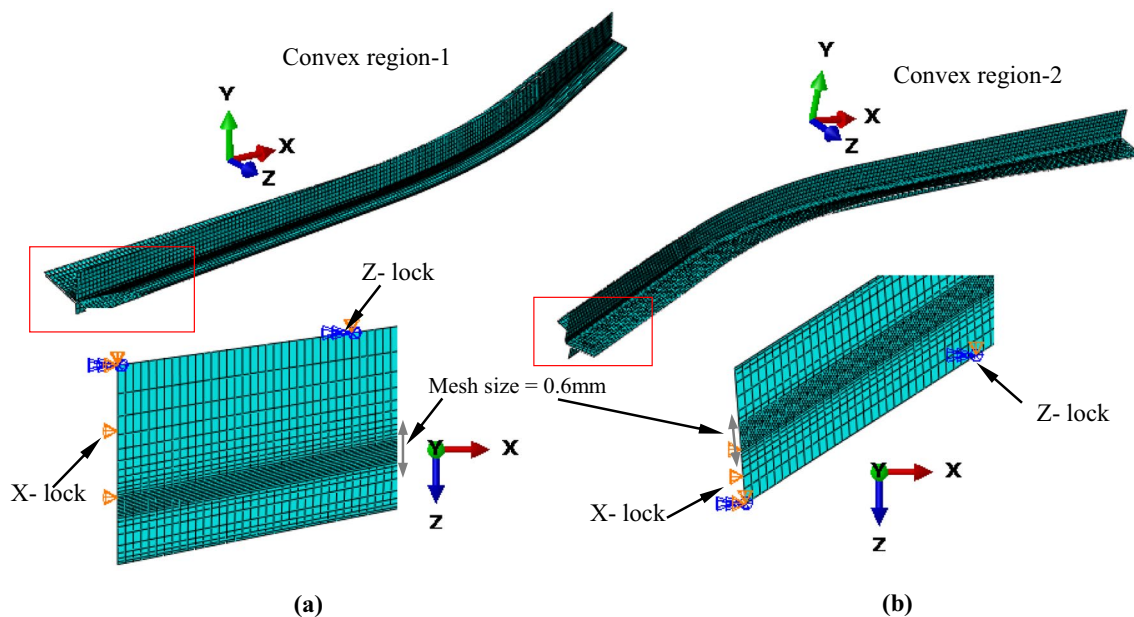

Fig. 21 The mesh and boundary conditions for the blank in (a) convex region-1 and (b) convex region-2

significantly higher load. Hence, the structural analysis of the formed component does not represent the ideal scenario since the formed part produced some twisting defects which is not considered in the optimisation analysis.

9 Discussion

The parametrisation description of long automotive structural parts can be achieved using our system of connected straight and curved profiles. The numerical examples in Section 7

(Cases 1 to 3) indicate that the newly presented parametrisation description can successfully find the final part shape with variable cross sections using only a few sets of design variables. The gradient-based method is selected as the optimiser because of the analytical sensitivities derived from our proposed parametrisation method. Given only a small number of design variables were utilised in the established optimisation platform, the number of iterations required to achieve the final optimised design is small, which reduced the computational cost.

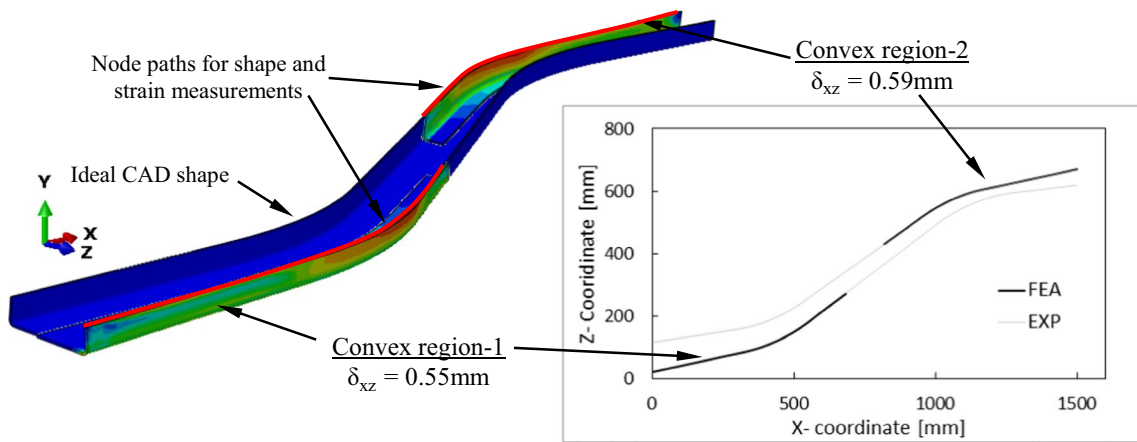The potential effectiveness and numerical stability of the proposed algorithm are exampled by the strain energy

Fig. 22 Shape from FEA vs ideal CAD shape

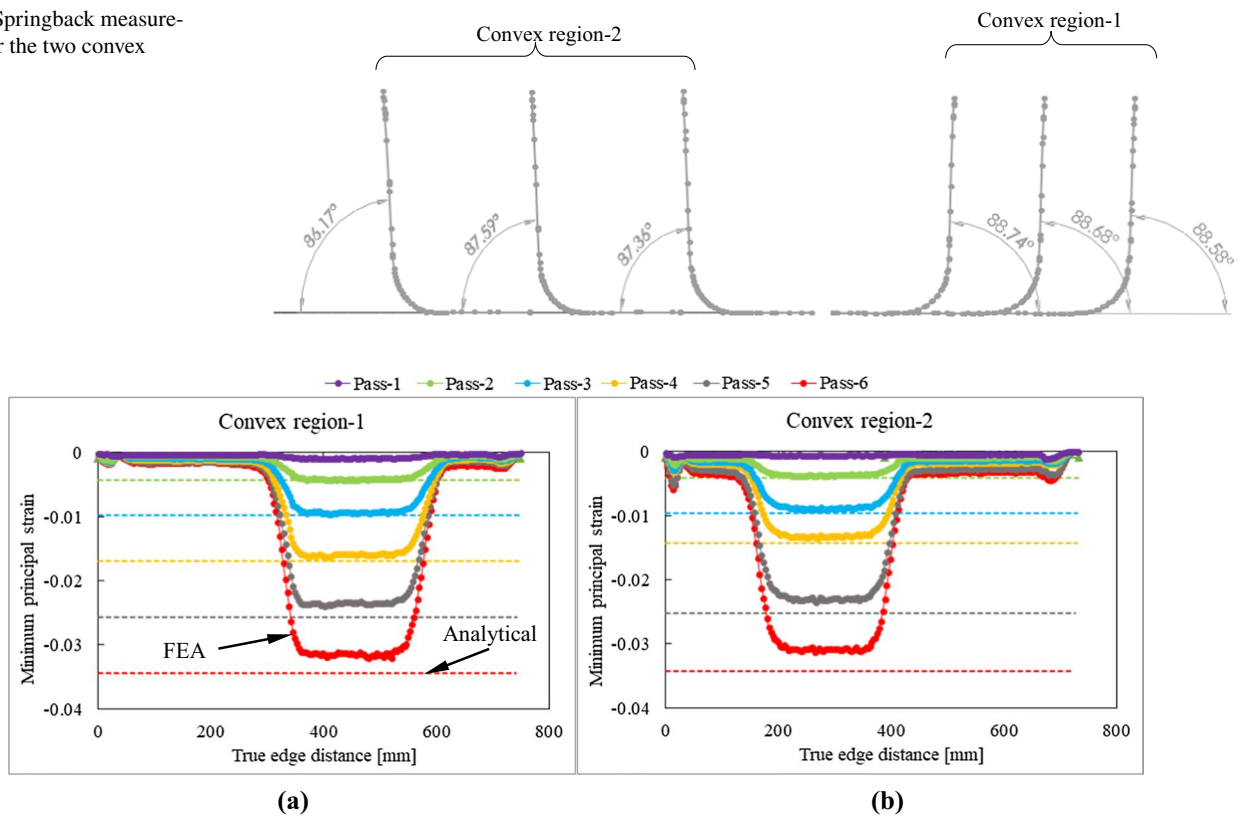**Fig. 23** Springback measurements for the two convex regions

Fig. 24 Minimum principal strain distribution along the flange edge for (a) convex region-1 and (b) convex region-2

decreasing monotonically during the optimisation process for all three chosen cases. With respect to Case 2, as the bending moment decreases from the fixed left end to the right end of the S-rail in the bending situation, this implies that the left-hand web end must widen during the optimisation process to decrease the strain energy. This has been shown by releasing the additional left end (yu_0) in the width direction in Case 3. The optimisation process of Case 3 leads to the left end becoming wider and the location of maximum stress moving towards the right end which becomes clear when comparing Fig. 18 (c) and (d).

It is noteworthy that the weight of the optimised S-rails is marginally lower compared to the initial design in all three
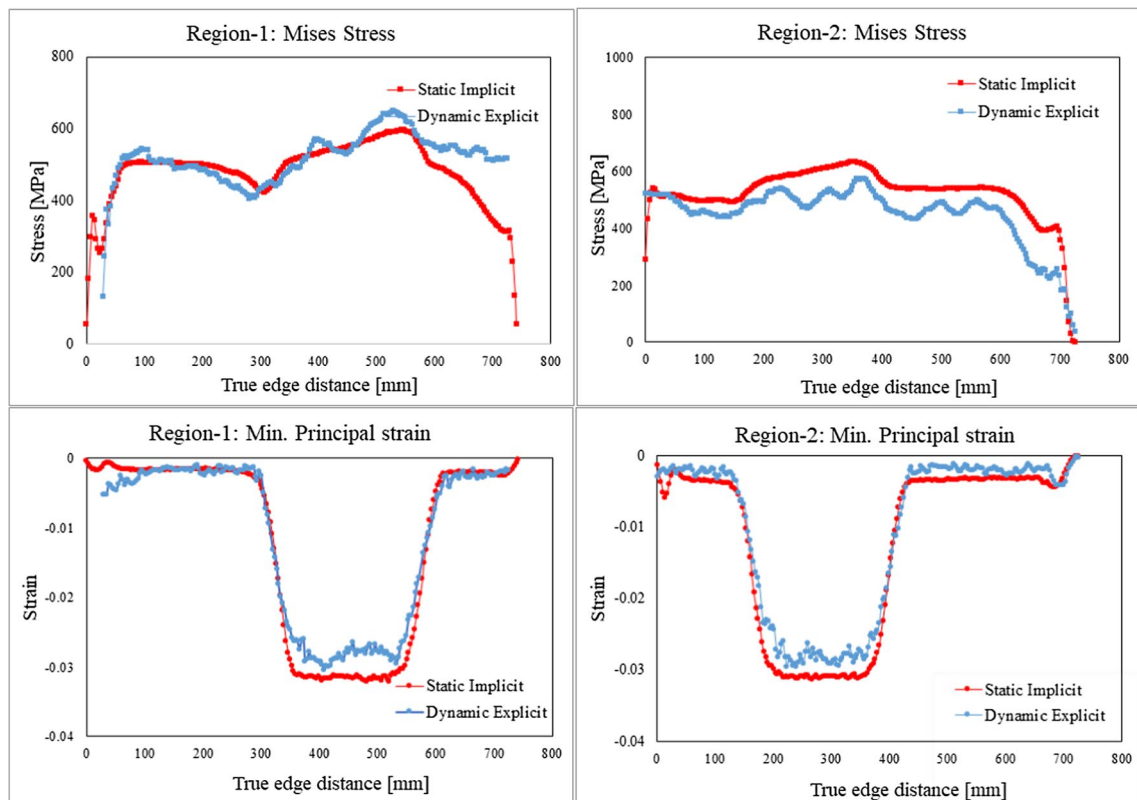
Fig. 25 Comparison of stress and strain between explicit and implicit results from the node paths of two critical convex regions after the final pass

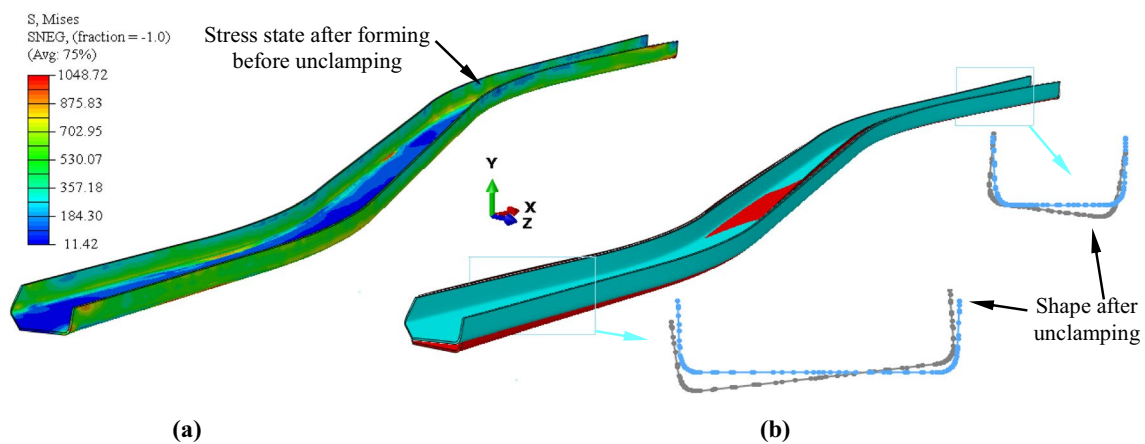**(a)**   **(b)**

Fig. 26 Deformed shapes from (a) the explicit analysis with Mises stress state before unclamping the sheet and (b) implicit analysis of sheet after unclamping with the twisted shape

presented case studies. This is due to the integrated area constraint being obeyed by the optimisation platform.

Although manufacturing constraints are included in the process, the results indicate that in some cases additional manufacturing constraints will be needed. The narrow width of the web section in the optimised design for Case 1 (refer to Table 2) would still cause manufacturing issues since the forming roll tools would not fit between the flanges at the minimum web width. Solving this issue would need an additional manufacturing constraint for a minimum web width.

Fig. 27 Applying bending load through punch contact.
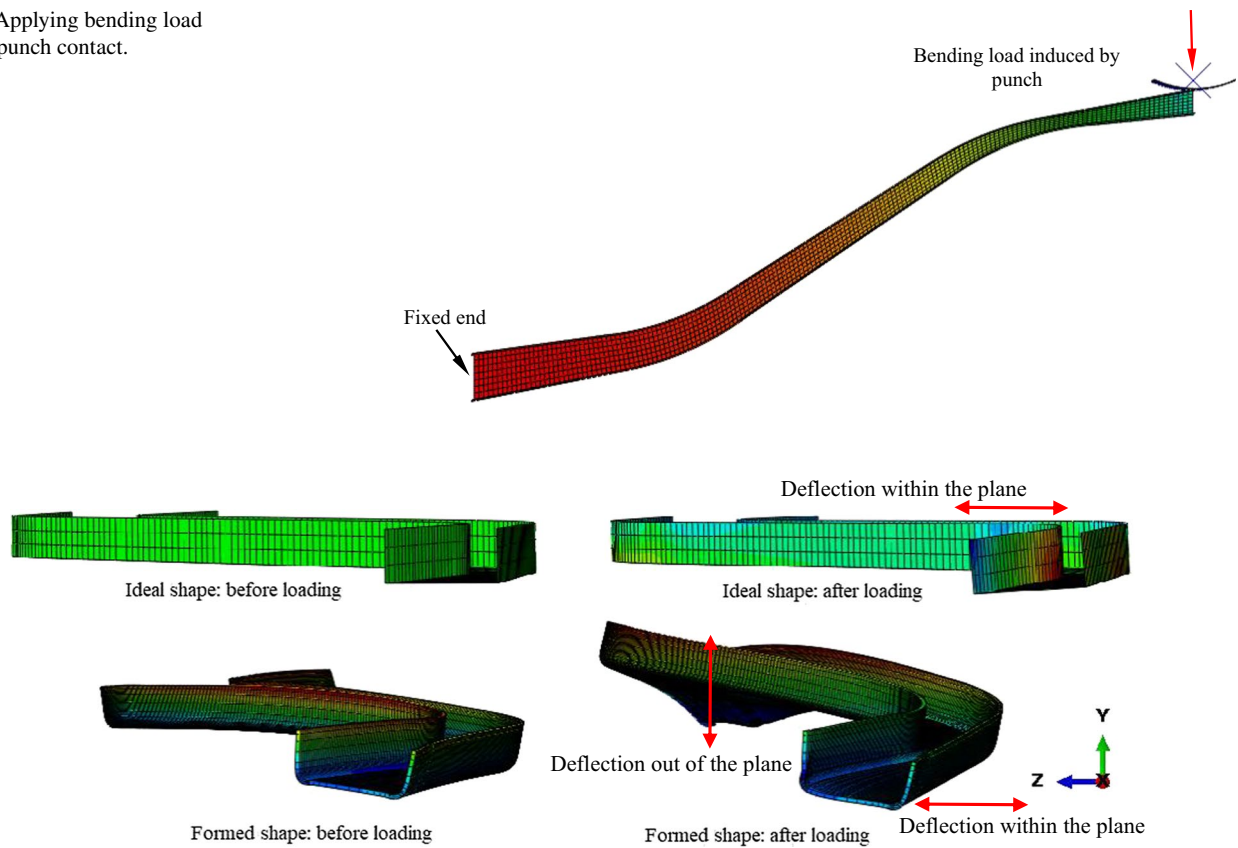

Fig. 28 Comparison of structural performance of optimised part and FRF formed part under bending load through punch contact

This constraint will need to be incorporated into a future optimisation method and can be created from an appropriate constraint on the profiles of the channels. Apart from this, it has been found that the residual stress from the FRF process may cause a small amount of twist after unclamping the formed structure. This twist can be formed out if an in-depth manufacturing process analysis was conducted, which still indicates that the optimised part is manufacturable. The amount of twist can be related to the amount of forming performed on each side of the channel. The twist can be estimated using the straight and curved profiles associated with the part, and thus will also need to be considered in future work.

Despite the advantages of the proposed method, it has to be also noted that there are some limitations. Most importantly, the proposed parametrisation is not able to automatically add additional curves to the initial input geometry. As mentioned in Section 2, the transitional curve can merge to one point, which enables the removal of unneeded transitional sections during the optimisation process. However, the current version does not support the ability to add more curved sections during the optimisation process. As the submitted geometry at the initial stage is usually based on the engineers' experience, it is therefore important to determine the input design variables of geometries, especially for complex loading and boundary conditions.

10 Conclusion

A new parametrisation method that uses a small number of design variables is proposed to capture shape configurations of channels with variable cross sections in width. The bend profile that the parameterisation method describes has been shown that it can estimate the forming strains in the part. This result can be used to manage the manufacturing constraints. We analytically derived the first order derivatives of the parameter driven variable width channel profiles. The derivatives that are calculated based on the proposed parametrisation method enable the utilisation of gradient-based optimisers. These optimisers require less iterations compared to gradient free methods to save the computational cost. An optimisation platform has been established based on the parametrisation and gradient-based Newton-like interior-point method and applied to the Flexible Roll Forming (FRF) process to test the optimisation platform. For this, the manufacturing constraints of FRF parts with variable cross section in width were integrated into the optimisation platform. As improving the stiffness of the structure would normally lead to increasing the weight, an area constraint of the structure was integrated. In addition, geometrical constraints were considered to avoid invalid shapes. Three optimisation cases were conducted to validate the parametrisation method,

as well as the effectiveness and general applicability of the platform. The concluding remarks are:

- The proposed parametrisation method successfully produced slender channels with width variants that maintained the manufacturing constraints, while only using a small set of design variables.
- Combined with a gradient-based optimisation, the parametrisation platform enables part shape optimisation with only a small number of the design variables. This significantly reduces the number of iterations and optimisation time.
- The new method successfully accounts for manufacturing constraints that are relevant to FRF to ensure the optimised part shapes can be successfully manufactured. The manufacturing constraints are based on ideal forming of the part, so it can be applied to other manufacturing processes.
- Part stiffness was increased by over 80% and the maximum stress was reduced by over 45% in some optimisation cases. This promises to improve the structural performance of an optimised part while maintaining the manufacturability of the final part shape.

Appendix A

The relationship between design variables(x_i, y_i, r_i) and intermediate variables $P_{i,j}(X_{i,j}, Y_{i,j})(j=0,1)$ can be categorised into several situations based on the sign of transitional radii and the values of adjacent coordinates in the y direction. One example is given in Fig. 29 to clarify this relationship.
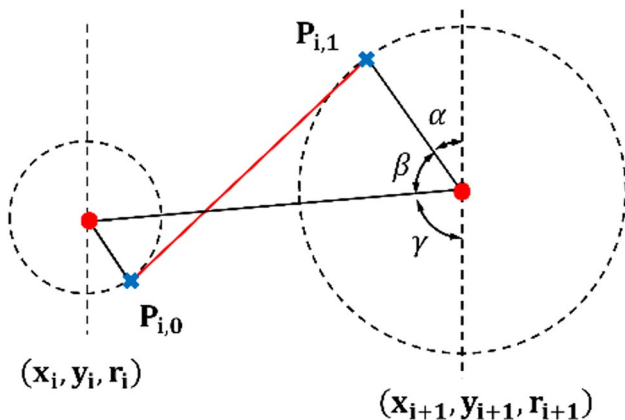

Fig. 29 Calculation of intermediate variables related to design variables

If $r_i < 0$, $r_{i+1} > 0$, and $y_i < y_{i+1}$, α is calculated by:

$$\alpha = \pi - \beta - \gamma \tag{27}$$

where

$$\beta = \cos^{-1} \frac{r_{i+1}}{\sqrt{\left(y_{i+1} - y_i\right)^2 + \left(x_{i+1} - x_i\right)^2}} \tag{28}$$

$$\gamma = \frac{\left|x_{i+1} - x_i\right|}{\left|y_{i+1} - y_i\right|} \ \left(y_{i+1} \neq y_i\right) \tag{29}$$

Substituting Eqs. (28) and (29) into Eq. (27) yields:

$$\alpha = \pi - \cos^{-1} \frac{r_{i+1}}{\sqrt{\left(y_{i+1} - y_i\right)^2 + \left(x_{i+1} - x_i\right)^2}} - \frac{\left|x_{i+1} - x_i\right|}{\left|y_{i+1} - y_i\right|} \left(y_{i+1} \neq y_i\right) \tag{30}$$

Using this angle, intermediate variables are defined as:

$$X_{i,0} = x_i + r_i \sin \alpha \tag{31}$$

$$Y_{i,0} = y_i - r_i \cos \alpha \tag{32}$$

$$X_{i,1} = x_{i+1} - r_{i+1} \sin \alpha \tag{33}$$

$$Y_{i,1} = y_{i+1} + r_{i+1} \cos \alpha \tag{34}$$

Sensitivity analysis of $\frac{\partial P_{i,j}}{\partial x_i}$ in Eq. (19) is decomposed as:

$$\frac{\partial P_{i,j}}{\partial x_i} = \begin{cases} \sum_{j=0}^{1} \frac{\partial X_{i,j}}{\partial x_i} + \frac{\partial Y_{i,j}}{\partial x_i} \ (i=0) \\ \sum_{j=0}^{1} \frac{\partial X_{i-1,j}}{\partial x_i} + \frac{\partial Y_{i-1,j}}{\partial x_i} + \frac{\partial X_{i,j}}{\partial x_i} + \frac{\partial Y_{i,j}}{\partial x_i} (i=1,\dots,n-1) \end{cases} \tag{35}$$

where $\frac{\partial X_{i,j}}{\partial x_i}$ and $\frac{\partial Y_{i,j}}{\partial x_i}$ are calculated through differentiating Eqs. (31-34). Sensitivities of intermediate variables with respect to design variables y_i and r_i are conducted using the same method.

Appendix B

The area of the channels can be calculated based on the intermediate variables ($P_{i,j}(X_{i,j}, Y_{i,j})(j=0,1)$), as shown in Fig. 6(a)-(c). Based on Fig. 4, the regular formulation of the web area is formed as:

$$S_w(X) = \begin{cases} \begin{aligned} &\sum_{i=0}^{n-1} \frac{(Y_{i,0}+Y_{i,1})(X_{i,1}-X_{i,0})}{2} + \\ &\sum_{j=1}^{n-1}\left\{\frac{(Y_{j-1,1}+Y_{j,0})(X_{j,0}-X_{j-1,1})}{2} - \frac{r_j^2\left[2\sin^{-1}\left(\frac{l_{P_{j-1,1},P_{j,0}}}{2|r_j|}\right)\right]-\sin\left[2\sin^{-1}\left(\frac{l_{P_{j-1,1},P_{j,0}}}{2|r_j|}\right)\right]}{2}\right\} \end{aligned} & (r_j < 0) \\[2em] \begin{aligned} &\sum_{i=0}^{n-1} \frac{(Y_{i,0}+Y_{i,1})(X_{i,1}-X_{i,0})}{2} + \\ &\sum_{j=1}^{n-1}\left\{\frac{(Y_{j-1,1}+Y_{j,0})(X_{j,0}-X_{j-1,1})}{2} + \frac{r_j^2\left[2\sin^{-1}\left(\frac{l_{P_{j-1,1},P_{j,0}}}{2|r_j|}\right)\right]-\sin\left[2\sin^{-1}\left(\frac{l_{P_{j-1,1},P_{j,0}}}{2|r_j|}\right)\right]}{2}\right\} \end{aligned} & (r_j > 0) \end{cases}$$

$$(36)$$

$$S_f(X) = \sum_{i=0}^{n-1}\left(\frac{(Y_{i,0}+Y_{i,1})(X_{i,1}-X_{i,0})}{2} + 2\sin^{-1}\left(\frac{l_{P_{i,1},P_{i+1,0}}}{2r_1}\right)r_{i+1}\right)h$$

$$(37)$$

where l is the chord length of the *ith* transitional section and h is the flange height shown in Fig. 6(d).

Data availability Not applicable.

Code availability Not applicable.

Declarations

Competing interest The authors have no relevant financial or non-financial interests to disclose.

Ethics approval Not applicable.

Consent to participate Not applicable.

Consent for publication Not applicable.

References

1. Sun G, Chen D, Zhu G, Li Q (2022) Lightweight hybrid materials and structures for energy absorption: A state-of-the-art review and outlook. Thin-Walled Struct. 172:108760. https://doi.org/10.1016/j.tws.2021.108760

2. Yun S, Kwon J, Cho W, Lee DC, Kim Y (2020) Performance improvement of hot stamping die for patchwork blank using mixed cooling channel designs with straight and conformal channels. Appl. Therm. Eng. 165:114562. https://doi.org/10.1016/j.applthermaleng.2019.114562

3. Ganapathy M, Li N, Lin J, Abspoel M, Bhattacharijee D (2019) Experimental investigation of a new low-temperature hot stamping process for boron steels. J. Adv. Manuf. Technol. 105:669–682. https://doi.org/10.1007/s00170-019-04172-5

4. Vinot P, Cogan S, Piranda J (2001) Shape optimization of thin-walled beam-like structures. Thin-Walled Struct. 39:611–630. https://doi.org/10.1016/S0263-8231(01)00024-6

5. Guillow SR, Lu G, Grzebieta RH (2001) Quasi-static axial compression of thin-walled circular aluminium tubes. Int. J. Mech. Sci. 43:2103–2123. https://doi.org/10.1016/S0020-7403(01)00031-5

6. Guler MA, Cerit ME, Bayram B, Gerceker B, Karakaya E (2010) The effect of geometrical parameters on the energy absorption characteristics of thin-walled structures under axial impact loading. Int J Crashworthiness 15:377–390. https://doi.org/10.1080/13588260903488750

7. Khalkhali A, Mostafapour M, Tabatabaie SM, Ansari B (2016) Multi-objective crashworthiness optimization of perforated square tubes using modified NSGAII and MOPSO. Struct. Multidisc. Optim. 54:45–61. https://doi.org/10.1007/s00158-015-1385-y

8. Hong W, Jin F, Zhou J, Xia Z, Xu Y, Yang L, Zheng Q, Fan H (2014) Quasi-static axial compression of triangular steel tubes. Thin-Walled Struct. 62:10–17. https://doi.org/10.1016/j.tws.2012.08.004

9. Abbasi M, Reddy S, Ghafari-Nazari A, Fard M (2015) Multi-objective crashworthiness optimization of multi-cornered thin-walled sheet metal members. Thin-Walled Struct. 89:31–41. https://doi.org/10.1016/j.tws.2014.12.009

10. Deng X, Liu W, Lin Z (2018) Experimental and theoretical study on crashworthiness of star-shaped tubes under axial compression. Thin-Walled Struct. 130:321–331. https://doi.org/10.1016/j.tws.2018.06.002

11. Fan Z, Lu G, Liu K (2013) Quasi-static axial compression of thin-walled tubes with different cross-sectional shapes. Eng. Struct. 55:80–89. https://doi.org/10.1016/j.engstruct.2011.09.020

12. Chen J, Li E, Li Q, Hou S, Han X (2022) Crashworthiness and optimization of novel concave thin-walled tubes. Compos. Struct. 283:115109. https://doi.org/10.1016/j.compstruct.2021.115109

13. Wu S, Sun G, Wu X, Li G, Li Q (2017) Crashworthiness analysis and optimization of fourier varying section tubes. Int. J. Non-Linear Mech. 92:41–58. https://doi.org/10.1016/j.ijnonlinmec.2017.03.001

14. Mamalis AG, Johnson W (1983) The quasi-static crumpling of thin-walled circular cylinders and frusta under axial compression. Int. J. Mech. Sci. 25:713–732. https://doi.org/10.1016/0020-7403(83)90078-4

15. Avalle M, Belingardi G, Chiandussi G, Vadori R (1997) Structural optimization of the axial crashing behaviour of thin walled tapered columns, In Computational Plasticity, Atti 5th International Conference on Computational Plasticity

16. Chiandussi G, Avalle M (2002) Maximisation of the crushing performance of a tubular device by shape optimization. Comput. Struct. 80:2425–2432. https://doi.org/10.1016/S0045-7949(02)00247-X

17. Qi C, Yang S, Dong FL (2012) Crushing analysis and multi objective crashworthiness optimization of tapered square tubes under

oblique impact loading. Thin-Walled Struct. 59:103–119. https://doi.org/10.1016/j.tws.2012.05.008

18. Zhang X, Zhang H, Wen Z (2015) Axial crushing of tapered circular tubes with graded thickness. Int. J. Mech. Sci. 92:12–23. https://doi.org/10.1016/j.ijmecsci.2014.11.022

19. Zhang X, Zhang H (2015) Relative merits of conical tubes with graded thickness subjected to oblique impact loads. Int. J. Mech. Sci. 98:111–125. https://doi.org/10.1016/j.ijmecsci.2015.04.013

20. Zhang H, Zhang X (2016) Crashworthiness performance of conical tubes with nonlinear thickness distribution. Thin-Walled Struct. 99:35–44. https://doi.org/10.1016/j.tws.2015.11.007

21. Zhang Y, Xu X, Sun G, Lai X, Li Q (2018) Nondeterministic optimization of tapered sandwich column for crashworthiness. Thin-Walled Struct. 122:193–207. https://doi.org/10.1016/j.tws.2017.09.028

22. Wang D, Jiang R, Wu Y (2016) A hybrid method of modified NSGA-II and TOPSIS for lightweight design of parameterized passenger car sub-frame. J. Mech. Sci. Technol. 30:4909–4917. https://doi.org/10.1007/s12206-016-1010-z

23. Zimmer H, Prabhuwaingankar M, Duddeck F (2009) Topology-and geometry based geometry-based structural optimization using implicit parametric model and LS-OPT, In 7th Europ. LS-DYNA Conf

24. Duddeck F, Zimmer H (2012) New achievements on implicit parameterization technique for combined shape and topology optimization for crashworthiness based on SEF-CONCEPT, Shape and Topology Optimziation for Crashworthiness, ICRASH2012

25. Rayamajhi M, Hunkeler S, Duddeck F (2014) Geometrical compatibility in structural shape optimisation for crashworthiness. Int. J. Crashworthiness. 19:42–56. https://doi.org/10.1080/13588265.2013.832720

26. Hilmann J, Paas M, Haenschke A, Vietor T (2007) Automatic concept model generation for optimisation and robust design of passenger cars. Adv. Eng. Softw. 38:795–801. https://doi.org/10.1016/j.advengsoft.2006.08.031

27. Duan L, Xiao NC, Hu Z, Li G, Cheng A (2017) An efficient lightweight design strategy for body-in-white based on implicit parameterization technique. Struct. Multidisc. Optim. 55:1927–1943. https://doi.org/10.1007/s00158-016-1621-0

28. Cai KF, Wang DF (2017) Optimizing the design of automotive S-rail using grey relational analysis coupled with grey entropy measurement to improve crashworthiness. Struct. Multidisc. Optim. 56:1539–1553. https://doi.org/10.1007/s00158-017-1728-y

29. Xie C, Wang DF (2020) Multi-objective cross-sectional shape and size optimization of S-rail using hybrid multi-criteria decision-making method. Struct. Multidisc. Optim. 62:3477–3492. https://doi.org/10.1007/s00158-020-02651-y

30. Yang L, Li BJ, Lv ZQ, Hou WB, Hu P (2016) Finite element mech deformation with the skeleton-section template. Comput. Aided Des. 73:11–25. https://doi.org/10.1016/j.cad.2015.11.002

31. Hu P, Yang L, Li BJ (2018) Skeleton-section template parameterization for shape optimization, J. Mech. Des. 140 121404-1 - 121404-10. https://doi.org/10.1115/1.4040487

32. Sigmund O (2011) On the usefulness of non-gradient approaches in topology optimization. Struct. Multidisc. Optim. 43:589–596. https://doi.org/10.1007/s00158-011-0638-7

33. Juan AA, Keenan P, Martí R, McGarraghy S, Panadero J, Carroll P, Oliva D (2023) A review of the role of heuristics in stochastic optimisation: from metaheuristics to learnheuristics. Ann Oper Res 320:831–861. https://doi.org/10.1007/s10479-021-04142-9

34. Wei RF, Pan G, Jiang J, Shen KC, Lyu D (2019) An efficient approach for stacking sequence optimization of symmetrical laminated composite cylindrical shells based on a genetic algorithm. Thin-Walled Struct. 142:160–170. https://doi.org/10.1016/j.tws.2019.05.010

35. Feng RL, Jiang JC, Sun ZC, Thakur A, Wei XZ (2021) A hybrid of genetic algorithm and particle swarm optimization for reducing material waste in extrusion-based additive manufacturing. Rapid Prototyp. J. 27:1872–1885. https://doi.org/10.1108/RPJ-11-2020-0292

36. Pirmohammad S, Esmaeili-Marzdashti S (2019) Multi-objective crashworthiness optimization of square and octagonal bitubal structures including different hole shapes. Thin-Walled Struct. 139:126–138. https://doi.org/10.1016/j.tws.2019.03.004

37. Nocedal J, Wright SJ (2006) Numerical Optimization, second ed., Springer

38. Sedlmaier A, Dietl T, Harrasser J (2017) 3D roll forming in automotive industry, In 5th International Conference on Steels in Cars and Trucks

39. Sedlmaier A, Dietl T (2018) 3D roll forming center for automotive applications. Procedia Manuf. 15:767–774. https://doi.org/10.1016/j.promfg.2018.07.319

40. Abeyrathna B, Abvabi A, Rolfe B, Taube R, Weiss M (2016) Numerical analysis of the flexible roll forming of an automotive component from high strength steel. IOP Conf. Ser.: Mater. Sci. Eng. 159:1–9. https://doi.org/10.1088/1757-899X/159/1/012005

41. Abeyrathna B, Ghanei S, Rolfe B, Taube R, Weiss M (2021) Optimising part quality in the flexible roll forming of an automotive component. Int. J. Adv. Manuf. Technol. 118:3361–3373. https://doi.org/10.1007/s00170-021-08176-y

42. Abeyrathna B, Rolfe B, Harrasser J, Sedlmaier A, Ge R, Pan L, Weiss M (2017) Prototyping of automotive components with variable width and depth. J. Phys.: Conf. Ser. 896:012092. https://doi.org/10.1088/1742-6596/896/1/012092

43. Kim D, Cha M, Kang Y (2017) Development of the bus frame by flexible roll forming. Procedia Eng. 183:11–16. https://doi.org/10.1016/j.proeng.2017.04.004

44. Larrañaga J, Berner S, Galdos L, Groche P (2011) Geometrical accuracy improvement in flexible roll forming lines. AIP Conf. Proc. 1315:557–562. https://doi.org/10.1063/1.3552505

45. Woo YY, Han SW, Oh IY, Moon YH (2019) Shape defects in the flexible roll forming of automotive parts. Int. J Automot. Technol. 20:227–236. https://doi.org/10.1007/s12239-019-0022-y

46. Berner S, Storbeck M, Groche P (2011) A study on flexible roll formed products accuracy by means of FEA and experimental tests. AIP Conf. Proc. 1353:345–350. https://doi.org/10.1063/1.3589539

47. Woo YY, Han SW, Hwang TW, Park JY, Moon YH (2018) Characterization of the longitudinal bow during flexible roll forming of steel sheets. J. Mater. Process. Technol. 252:782–794. https://doi.org/10.1016/j.jmatprotec.2017.10.048

48. Park JC, Yang DY, Cha MH, Kim DG, Nam JB (2014) Investigation of a new incremental counter forming in flexible roll forming to manufacturing accurate profiles with variable cross-sections. Int. J. Mach. 86:68–80. https://doi.org/10.1016/j.ijmachtools.2014.07.001

49. Yan Y, Nie HZ, Wang HB, Li Q, Liu YF (2017) A novel roll-die forming technology and its FEM simulation. Procedia Eng. 207:1302–1307. https://doi.org/10.1016/j.proeng.2017.10.887

50. Groche P, Zettler A, Berner S, Schneider G (2011) Development and verification of a one-step-model for the design of flexible roll formed parts. Int. J. Mater. Form. 4:371–377. https://doi.org/10.1007/s12289-010-0998-3

51. Kasaei MM, Naeini HM, Abbaszadeh B, Mohammadi M, Ghodsi M, Kiuchi M, Zolghadr R, Liaghat G, Tafti RA, Tehrani MS (2014) Flange wrinkling in flexible roll forming process. Procedia Eng. 81:245–250. https://doi.org/10.1016/j.proeng.2014.09.158

52. Jiao JS, Rolfe B, Mendiguren J, Weiss M (2015) An analytical approach to predict web-warping and longitudinal stain in flexible roll formed sections of variable width. Int. J. Mech. Sci. 90:228–238. https://doi.org/10.1016/j.ijmecsci.2014.11.010

53. Jiao JS, Rolfe B, Mendiguren J, Weiss M (2016) An analytical model for web-warping in variables width flexible roll forming. Int. J. Adv. Manuf. Technol. 86:1545–1555. https://doi.org/10.1007/s00170-015-8191-y

54. Rezaei R, Naeini HH, Tafti RA, Kasaei MM, Mohammadi M, Abbaszadeh B (2017) Effect of bend curve on web warping in flexible roll formed profiles. Int. J. Adv. Manuf. Technol. 93:3625–3636. https://doi.org/10.1007/s00170-017-0784-1

55. Asl YD, Woo YY, Kim Y, Moon YH (2020) Non-sorting multi-objective optimization of flexible roll forming using artificial neural networks. Int. J. Adv. Manuf. Technol. 107:2875–2888. https://doi.org/10.1007/s00170-020-05209-w

56. Kasaei MM, Naeini HM, Abbaszadeh B, Roohi AH, Silva MB, Martins PAF (2021) On the prediction of wrinkling in flexible roll forming. Int. J. Adv. Manuf. Technol. 113:2257–2275. https://doi.org/10.1007/s00170-021-06790-4

57. Paralikas J, Salonitis K, Chryssolouris G (2013) Robust optimization of the energy efficiency of the cold roll forming process. Int. J. Adv. Manuf. Technol. 69:461–481. https://doi.org/10.1007/s00170-013-5011-0

58. Gavin HP (2015) Strain energy in linear elastic solids. Department of Civil and Environmental Engineering, Duke University: Durham, NC, USA. https://people.duke.edu/~hpgavin/cee201/strain-energy.pdf

59. Makris PA, Provatidis CG, Venetsanos DT (2006) Structural optimization of thin-walled tubular trusses using a virtual strain energy density approach. Thin-Walled Struct. 44:235–246. https://doi.org/10.1016/j.tws.2006.01.005

60. Ghabraie K (2015) The ESO method revisited. Struct. Multidisc. Optim. 51:1211–1222. https://doi.org/10.1007/s00158-014-1208-6

61. Fu YF, Rolfe B, Chiu LN, Wang Y, Huang X, Ghabraie K (2020) SEMDOT: Smooth-edged material distribution for optimizing topology algorithm. Adv. Eng. Softw. 150:102921. https://doi.org/10.1016/j.advengsoft.2020.102921

62. Herskovits J (1995) A View on Nonlinear Optimization, in: Adv. Struct. Optim., Herskovits J. (Eds.), Solid Mechanics and Its Applications, 22 71-116. https://doi.org/10.1007/978-94-011-0453-1_3

63. Zhou Y, Lan F, Chen J (2011) Crashworthiness research on S-shaped front rails made of steel–aluminium hybrid materials. Thin-Walled Struct. 49:291–297. https://doi.org/10.1016/j.tws.2010.10.007

64. Marciniak Z, Duncan JL, Hu SJ (2002) Mechanics of Sheet Metal Forming. Elsevier

65. Hosseini SM, Rad MA, Khalkhali A (2019) Optimal design of the S-rail family for an automotive platform with novel modifications on the product-family optimization process. Thin-Walled Struct. 138:143–154. https://doi.org/10.1016/j.tws.2019.01.046

66. Abeyrathna B, Rolfe B, Hodgson PD, Weiss M (2014) An experimental investigation of edge strain and bow in roll forming a V-section. Mater. Sci. Forum. 773:153–159. https://doi.org/10.4028/www.scientific.net/MSF

67. Sreenivas A, Abeyrathna B, Rolfe B, Weiss M (2022) Longitudinal strain and wrinkling analysis of variable depth flexible roll forming. J. Manuf. Process. 81:414–432. https://doi.org/10.1016/j.jmapro.2022.06.063